

Evaluating Precipitation Distributions at Regional Scales: A Benchmarking Framework and Application to CMIP 5 and 6 Models

Min-Seop Ahn^{1,2,3,*}, Paul A. Ullrich^{1,4}, Peter J. Gleckler¹, Jiwoo Lee^{1,*}, Ana C. Ordonez¹,
and Angeline G. Pendergrass^{5,6}

¹*PCMDI, Lawrence Livermore National Laboratory, Livermore, CA, USA*

²*NASA Goddard Space Flight Center, Greenbelt, MD, USA*

³*ESSIC, University of Maryland, College Park, MD, USA*

⁴*Department of Land, Air and Water Resources, University of California, Davis, CA, USA*

⁵*Earth and Atmospheric Science, Cornell University, Ithaca, NY, USA*

⁶*National Center for Atmospheric Research, Boulder, CO, USA*

June 2023

Revised

Geoscientific Model Development

* Corresponding author: Min-Seop Ahn (ahn6@llnl.gov) and Jiwoo Lee (lee1043@llnl.gov)

1 **Abstract**

2 As the resolution of global Earth system models increases, regional scale evaluation is
3 becoming ever more important. This study presents a framework for quantifying
4 precipitation distributions at regional scales and applies it to evaluate CMIP 5 and 6
5 models. We employ the IPCC AR6 climate reference regions over land and propose
6 refinements to the oceanic regions based on the homogeneity of precipitation distribution
7 characteristics. The homogeneous regions are identified as heavy, moderate, and light
8 precipitating areas by K-means clustering of IMERG precipitation frequency and amount
9 distributions. With the global domain partitioned into 62 regions, including 46 land and 16
10 ocean regions, we apply 10 established precipitation distribution metrics. The collection
11 includes metrics focused on the maximum peak, lower 10th percentile, and upper 90th
12 percentile in precipitation amount and frequency distributions, the similarity between
13 observed and modeled frequency distributions, an unevenness measure based on
14 cumulative amount, average total intensity on all days with precipitation, and number of
15 precipitating days each year. We apply our framework to 25 CMIP5 and 41 CMIP6
16 models, and 6 observation-based products of daily precipitation. Our results indicate that
17 many CMIP 5 and 6 models substantially overestimate the observed light precipitation
18 amount and frequency as well as the number of precipitating days, especially over mid-
19 latitude regions outside of some land regions in the Americas and Eurasia. Improvement
20 from CMIP 5 to 6 is shown in some regions, especially in mid-latitude regions, but it is not
21 evident globally, and over the tropics most metrics point toward degradation.

22 **1. Introduction**

23 Precipitation is a fundamental characteristic of the Earth's hydrological cycle and one that
24 can have large impacts on human activity. The impact of precipitation depends on its
25 intensity and frequency characteristics (e.g., Trenberth et al. 2003; Sun et al. 2006;
26 Trenberth and Zhang 2018). Even with the same amount of precipitation, more intense
27 and less frequent rainfall is more likely to lead to extreme precipitation events such as
28 floods and drought compared to less intense and more frequent rainfall. While mean
29 precipitation has improved in Earth system models, the precipitation distributions continue
30 to have biases (e.g., Dai 2006; Fiedler et al. 2020), which limits the utility of these
31 simulations, especially at the level of accuracy that is increasingly demanded in order to
32 anticipate and adapt to changes in precipitation due to global warming.

33

34 Multi-model intercomparison with a well-established diagnosis framework facilitates
35 identifying common model biases and sometimes yields insights into how to improve
36 models. The Coupled Model Intercomparison Project (CMIP; Meehl et al. 2000, 2005,
37 2007; Taylor et al. 2012; Eyring et al. 2016) is a well-established experimental protocol to
38 intercompare state-of-the-art Earth system models, and the number of models and
39 realizations participating in CMIP has been growing through several phases from 1
40 (Meehl et al. 2000) to 6 (Eyring et al. 2016). Given the increasing number of models,
41 developed at higher resolution and with increased complexity, modelers and analysts
42 could benefit from capabilities that help synthesize the consistency between observed
43 and simulated precipitation. As discussed in previous studies (e.g., Abramowitz 2012),
44 our reference to model benchmarking implies model evaluation with community-

45 established reference data sets, performance tests (metrics), variables, and spatial and
46 temporal resolutions. The U.S. Department of Energy (DOE) envisioned a framework for
47 both baseline and exploratory precipitation benchmarks (U.S. DOE. 2020) as summarized
48 by Pendergrass et al. (2020). While the exploratory benchmarks focus on process-
49 oriented and phenomena-based metrics at a variety of spatiotemporal scales (Leung et
50 al. 2022), the baseline benchmarks target well-established measures such as mean state,
51 the seasonal and diurnal cycles, variability across timescales, intensity/frequency
52 distributions, extremes, and drought (e.g., Gleckler et al. 2008; Covey et al. 2016; Wehner
53 et al. 2020; Ahn et al. 2022). The current study builds on the baseline benchmarks by
54 proposing a framework for benchmarking simulated precipitation distributions against
55 multiple observations using well-established metrics and reference regions. To ensure
56 consistent application of this framework, the metrics used herein are implemented and
57 made available as part of the widely-used Program for Climate Model Diagnosis and
58 Intercomparison (PCMDI) metrics package.

59

60 Diagnosing precipitation distributions and formulating metrics that extract critical
61 information from precipitation distributions have been addressed in many previous
62 studies. Pendergrass and Deser (2017) proposed several precipitation distribution
63 metrics based on frequency and amount distribution curves. The precipitation frequency
64 distribution quantifies how often rain occurs at different rain rates, whereas the
65 precipitation amount distribution quantifies how much rain falls at different rain rates.
66 Based on the distribution curves, Pendergrass and Deser (2017) extracted rain frequency
67 peak and amount peak where the maximum non-zero rain frequency and amount occur,

68 respectively. Pendergrass and Knutti (2018) introduced a metric that measures the
69 unevenness of daily precipitation based on the cumulative amount curve. Their
70 unevenness metric is defined as the number of wettest days that constitute half of the
71 annual precipitation. In the median of station observations equatorward of 50° latitude,
72 half of the annual precipitation falls in only about the heaviest 12 days, and generally
73 models underestimate the observed unevenness (Pendergrass and Knutti 2018). In
74 addition, several metrics have been developed to distill important precipitation
75 characteristics, such as the fraction of precipitating days and simple daily intensity index
76 (SDII, Zhang et al. 2011). In this study we implement all these well-established metrics
77 and several other complementary metrics into our framework.

78

79 Many studies have analyzed the precipitation distributions over large domains (e.g., Dai
80 2006; Pendergrass and Hartmann 2014; Ma et al. 2022). Often, these domains comprise
81 both heavily precipitating and dry regions. Given the emphasis on regional scale analysis
82 continues to grow as models' horizontal resolution increases, interpretation of domain-
83 averaged distributions could be simplified by defining regions that are not overly complex
84 or heterogeneous in terms of their precipitation distribution characteristics. Iturbide et al.
85 (2020) has identified climate reference regions that have been adopted in the sixth
86 assessment report (AR6) of the Intergovernmental Panel on Climate Change (IPCC). Our
87 framework is based on these IPCC AR6 reference regions for objective examination of
88 precipitation distributions over land. Over the ocean we have revised some of the regions
89 of Iturbide et al. (2020) to better isolate homogeneous precipitation distribution
90 characteristics.

91
92 In this study, we propose a modified IPCC AR6 reference regions and a framework for
93 regional scale quantification of simulated precipitation distributions, which is implemented
94 into the PCMDI metrics package to enable researchers to readily use the metric collection
95 in a common framework. The remainder of the paper is organized as follows: Sections 2
96 and 3 describe the data and analysis methods. Section 4 presents results including the
97 application and modification of IPCC AR6 climate reference regions, evaluation of CMIP
98 5 and 6 models with multiple observations, and their improvement across generations.
99 Sections 5 and 6 discuss and summarize the main accomplishments and findings from
100 this study.

101
102
103 **2. Data**

104 2.1. Observational data
105 For reference data, we use six global daily precipitation products first made available as
106 part of the Frequent Rainfall Observations on GridS (FROGS) database (Roca et al.,
107 2019) and then further aligned with CMIP output via the data specifications of the
108 Observations for Model Intercomparison Project (Obs4MIPs, Waliser et al. 2020). These
109 include five satellite-based products and a recent atmospheric reanalysis product. The
110 satellite-based precipitation products include the Integrated Multi-satellitE Retrievals for
111 GPM version 6 final run product (Huffman et al. 2020; hereafter IMERG), the Tropical
112 Rainfall Measuring Mission Multi-satellite Precipitation Analysis 3B42 version 7 product
113 (Huffman et al. 2007; hereafter TRMM), the bias-corrected Climate Prediction Center

114 Morphing technique product (Xie et al. 2017; hereafter CMORPH), the Global
115 Precipitation Climatology Project 1DD version 1.3 (Huffman et al. 2001; hereafter GPCP),
116 and Precipitation Estimation from Remotely Sensed Information using Artificial Neural
117 Networks (Ashouri et al. 2015; hereafter PERSIANN). The reanalysis product included
118 for context is the European Centre for Medium-Range Weather Forecasts (ECMWF)'s
119 fifth generation of atmospheric reanalysis (Hersbach et al. 2020; hereafter ERA5). Table
120 1 summarizes the observational datasets with the data source, coverage of domain and
121 period, resolution of horizontal space and time frequency, and references. We use the
122 data periods available via FROGS and Obs4MIPs as follows: 2001-2020 for IMERG,
123 1998-2018 for TRMM, 1998-2012 for CMORPH, 1997-2020 for GPCP, 1984-2018 for
124 PERSIANN, and 1979-2018 for ERA5.

125

126 2.2. CMIP model simulations

127 We analyze daily precipitation from all realizations of AMIP simulations available from
128 CMIP5 (Taylor et al. 2012) and CMIP6 (Eyring et al. 2016). We have chosen to
129 concentrate our analysis on AMIP simulations rather than the coupled Historical
130 simulations because the simulated precipitation in the latter is strongly influenced by
131 biases in the modeled sea surface temperature, complicating any interpretation regarding
132 the underlying causes of the precipitation errors. Table 2 lists the participating models,
133 the number of realizations, and the horizontal resolution in each modeling institute. We
134 evaluate the most recent 20 years (1985-2004) that both CMIP 5 and 6 models have in
135 common for a fair comparison with satellite-based observations.

136

137

138 **3. Methods**

139 In our framework we apply 10 metrics that characterize different and complementary
140 aspects of the intensity distribution of precipitation at regional scales. Table 3 summarizes
141 the metrics including their definition, purpose, and references. The computation of the
142 metrics has been implemented and applied in the PCMDI metrics package (PMP;
143 Gleckler et al. 2008, 2016).

144

145 3.1. Frequency and amount distributions

146 Following Pendergrass and Hartmann (2014) and Pendergrass and Deser (2017), we use
147 logarithmically-spaced bins of daily precipitation to calculate both the precipitation
148 frequency and amount distributions. Each bin is 7% wider than the previous one, and the
149 smallest non-zero bin is centered at 0.03 mm/day. The frequency distribution is the
150 number of days in each bin normalized by the total number of days, and the amount
151 distribution is the sum of accumulated precipitation in each bin normalized by the total
152 number of days. Based on these distributions (Fig. 1a), we identify the rain rate where the
153 maximum peak of the distribution appears (Amount/Frequency Peak, Pendergrass and
154 Deser 2017; also called mode, Kooperman et al., 2016) and formulate several
155 complementary metrics that measure the fraction of the distribution lower 10 percentile
156 (P10) and upper 90 percentile (P90). The precipitation bins less than 0.1 mm/day are
157 considered dry for the purpose of these calculations. The threshold rain rates for 10th and
158 90th percentiles are defined from the amount distribution as determined from
159 observations. Here we use IMERG as the default reference observational dataset. The

160 final frequency related metric we employ is the Perkins score, which measures the
161 similarity between observed and modeled frequency distributions (Perkins et al. 2007).
162 With the sum of a frequency distribution across all bins being unity, the Perkins score is
163 defined as the sum of minimum values between observed and modeled frequency across
164 all bins: $Perkins\ Score = \sum_1^n \text{minimum}(Z_o, Z_m)$ where n is the number of bins, Z_o and Z_m
165 are the frequency in a given bin for observation and model, respectively. The Perkins
166 score is a unitless scalar varying from 0 (low similarity) to 1 (high similarity).

167

168 3.2. Cumulative fraction of annual precipitation amount

169 Following Pendergrass and Knutti (2018), we calculate the cumulative sum of daily
170 precipitation each year sorted in descending order (i.e., wettest to driest) and normalized
171 by the total precipitation for that year. From the distribution for each individual year (see
172 Fig. 1b), we obtain the metrics gauging the number of wettest days for half of annual
173 precipitation (Unevenness, Pendergrass and Knutti 2018) and the fraction of the number
174 of precipitating ($\geq 1\text{mm/day}$) days (FracPRdays). To facilitate comparison against longer-
175 established analyses (e.g., ETCCDI, Zhang et al., 2011), we include the daily
176 precipitation intensity, calculated by dividing the annual total precipitation by the number
177 of precipitating days (SDII, Zhang et al. 2011). To obtain values of these metrics over
178 multiple years, we take the median across years following Pendergrass and Knutti (2018;
179 for unevenness).

180

181 3.3. Reference regions

182 We use the spatial homogeneity of precipitation characteristics as a basis for defining
183 regions, as in previous studies (e.g., Swenson and Grotjahn 2019). In addition to
184 providing more physically-based results, this also simplifies interpretation with robust
185 diagnostics when we average a distribution characteristic across the region. We use K-
186 means clustering (MacQueen 1967) with the concatenated frequency and amount
187 distributions of IMERG over the global domain to identify homogeneous regions for
188 precipitation distributions. K-means clustering is an unsupervised machine learning
189 algorithm that separates characteristics of a dataset into a given number of clusters
190 without explicitly provided criteria. This method has been widely used because it is faster
191 and simpler than other methods. Here, we use 3 clusters to define heavy, moderate and
192 light precipitation regions. Figure 2 shows the spatial pattern of IMERG precipitation mean
193 state and clustering results defining heavy (blue), moderate (green), and light (orange)
194 precipitation regions. The spatial pattern of these clustering regions resembles the pattern
195 of the mean state of precipitation, providing a sanity check indicating that the cluster-
196 based regions are physically reasonable. Note that the clustering result with frequency
197 and amount distributions is not significantly altered if we incorporate cumulative amount
198 fraction. However, the inclusion of the cumulative amount fraction to the clustering yields
199 a slightly noisier pattern, and thus we have chosen to use the clustering result only with
200 frequency and amount distributions.

201
202 In support of the AR6, the IPCC proposed a set of climate reference regions (Iturbide et
203 al. 2020). These regions were defined based on geographical and political boundaries
204 and the climatic consistency of temperature and precipitation in current climate and

205 climate change projections. When defining regions, the land regions use both information
206 from current climate and climate change projections, while the ocean regions use only
207 the information from climate change projections. In other words, the climatic consistency
208 of precipitation in the current climate is not explicitly represented in the definition of the
209 oceanic regions. Figure 3a shows the IPCC AR6 climate reference regions superimposed
210 on our precipitation clustering regions shown in Fig. 2b. The land regions correspond
211 reasonably well to the clustering regions, but some ocean regions are too broad, including
212 both heavy and light precipitating regions (Fig. 3a). In this study, the ocean regions are
213 modified based on the clustering regions, while the land regions remain the same as in
214 the AR6 (Fig. 3b).

215

216 In the Pacific Ocean region, the original IPCC AR6 regions consist of equatorial Pacific
217 Ocean (EPO), northern Pacific Ocean (NPO), and southern Pacific Ocean (SPO). Each
218 of these regions includes areas of both heavy and light precipitation. EPO includes the
219 Intertropical Convergence Zone (ITCZ), the South Pacific Convergence Zone (SPCZ),
220 and also the dry southeast Pacific region. The NPO region includes the north Pacific storm
221 track and the dry northeast Pacific. The SPO region includes the southern part of SPCZ
222 and the dry southeast area of the Pacific. In our modified IPCC AR6 regions, the Pacific
223 Ocean region is divided into four heavy precipitating regions (NPO, NWPO, PITCZ, and
224 SWPO) and two light and moderate precipitating regions (NEPO and SEPO). Similarly,
225 in the Atlantic Ocean region, the original IPCC AR6 regions consist of the equatorial
226 Atlantic Ocean (EAO), northern Atlantic Ocean (NAO), and southern Atlantic Ocean
227 (SAO), with each including both heavy and light precipitating regions. Our modified

228 Atlantic Ocean region consists of two heavy precipitating regions (NAO and AITCZ) and
229 two light and moderate precipitating regions (NEAO and SAO). The Indian Ocean (IO)
230 region is not modified as the original IPCC AR6 climate reference region separates well
231 the heavy precipitating equatorial IO (EIO) region from the moderate and light
232 precipitating southern IO (SIO) region. The Southern Ocean (SOO) is modified to mainly
233 include the heavy precipitation region around the Antarctic. The original IPCC AR6
234 climate reference regions consist of 58 regions including 12 oceanic regions and 46 land
235 regions, while our modification consists of 62 regions including 16 oceanic regions and
236 the same land regions as the original (see Table 4). Note that the Caribbean (CAR), the
237 Mediterranean (MED), and Southeast Asia (SEA) are not counted for the oceanic regions.

238

239 3.4. Evaluating model performance

240 We use two simple measures to compare the collection of CMIP 5 and 6 model
241 simulations with the five satellite-based observational products (IMERG, TRMM,
242 CMORPH, GPCP, and PERSIANN). One gauges how many models within the multi-
243 model ensemble fall within the observational range between the minimum and maximum
244 observed values for each metric and each region. Another is how many models
245 underestimate or overestimate all observations, i.e., are outside the bounds spanned by
246 the minimum and maximum values across the five satellite-based products. To quantify
247 the dominance of underestimation versus overestimation of the multi-model ensemble
248 with a single number, we use the following measure formulation: $(nO - nU)/nT$ where nO
249 is the number of overestimating models, nU is the number of underestimating models,
250 and nT is the total number of models. Thus, positive values represent overestimation, and

251 negative values represent underestimation. If models are mostly within the observational
252 range or widely distributed from underestimation to overestimation, the quantification
253 value would approach zero.

254

255 Many metrics that can be used to characterize precipitation, including those used here,
256 are sensitive to the spatial and temporal resolutions at which the model and observational
257 data are analyzed (e.g., Pendergrass and Knutti 2018, Chen and Dai 2019). As in many
258 previous studies the diagnosis of precipitation in CMIP 5 and 6 models (e.g., Fiedler et al.
259 2020; Tang et al. 2021; Ahn et al. 2022), to ensure appropriate comparisons, we conduct
260 all analyses at a common horizontal grid of 2x2 degrees with a conservative regridding
261 method. For models with multiple ensemble members, we first compute the metrics for
262 all available realizations and then average the results across the realizations.

263

264

265 **4. Results**

266 4.1. Homogeneity within reference regions

267 For the regional scale analysis, we employ the IPCC AR6 climate reference regions
268 (Iturbide et al. 2020) while we revise the region dividings over the oceans based on
269 clustered precipitation characteristics as described in section 3.3. To quantitatively
270 evaluate the homogeneity of precipitating distributions in the reference regions, we use
271 three homogeneity metrics: the Perkins score (Perkins et al. 2007), Kolmogorov–Smirnov
272 test (K-S test, Chakravart et al. 1967), and Anderson-Darling test (A-D test, Stephens
273 1974). The three metrics measure the similarity between the regionally-averaged and

274 individual grid cell frequency distributions within the region. The Perkins score measures
275 the overall similarity between two frequency distributions, which is one of our distribution
276 performance metrics described in Section 3.1. The K-S and A-D tests focus more on the
277 similarity in the center and the side of the frequency distribution, respectively. The three
278 homogeneity metrics could complement each other as their main focuses are on different
279 aspects of frequency distributions.

280

281 In the original IPCC AR6 reference regions, the oceanic regions show relatively low
282 homogeneity of precipitating characteristics compared to land regions (Fig. 4). The Pacific
283 and Atlantic Ocean regions show much lower homogeneity than the Indian Ocean,
284 especially in EPO and EAO regions. In the modified oceanic regions, the homogeneities
285 show an overall improvement with the three homogeneity metrics. In particular, the
286 homogeneity over the heavy precipitating regions where the homogeneity was lower (e.g.,
287 Pacific and Atlantic ITCZ and mid-latitude storm track regions) are largely improved. The
288 clustering regions shown here are obtained based on IMERG precipitation. However,
289 since different satellite-based products show substantial discrepancies in precipitation
290 distributions, it is important to assess whether the improved homogeneity in the modified
291 regions is similarly improved across other different datasets. Figure 5 shows the
292 homogeneity of precipitation distribution characteristics for different observational
293 datasets using the Perkins score. Although the region modifications we have made are
294 based on the clustering regions of IMERG precipitation, Fig. 5 suggests that the
295 improvement of the homogeneity over the modified regions is consistent across different
296 observational datasets. We further tested the homogeneity for different seasons (see Fig.

297 S1 in the supplement material). The homogeneity is overall improved in the modified
298 regions across the seasons even though we defined the reference regions based on
299 annual data.

300

301 4.2. Regional evaluation of model simulations against multiple observations
302 The precipitation distribution metrics used in this study are mainly calculated from three
303 curves: amount distribution, frequency distribution, and cumulative amount fraction
304 curves. Figure 6 shows these curves for three selected regions based on the clustered
305 precipitating characteristics (NWPO, which is a heavy precipitation dominated ocean
306 region; SEPO, a light precipitation dominated ocean region; and ENA, a heavy
307 precipitation dominated land region). The heavy and light precipitating regions are well
308 distinguished by their overlaid distribution curves. The amount distribution has a
309 distinctive peak in the heavy precipitating region (Figs. 6a and 6g), while it is flatter in the
310 light precipitating region (Fig. 6d). The frequency distribution is more centered on the
311 heavier precipitation side in the heavy precipitating region (Figs. 6b, 6h) than in the light
312 precipitating region (Fig. 6e). The cumulative fraction increases more steeply in the light
313 precipitating region (Fig. 6f) than in the heavy precipitating region (Figs. 6c and 6i),
314 indicating there are fewer precipitating days in the light precipitating region. NWPO and
315 SEPO were commonly averaged for representing the tropical ocean region in many
316 studies, but these different characteristics in the precipitation distributions demonstrate
317 the additional information available via a regional scale analysis. Although satellite-based
318 observations are less reliable over the light precipitating ocean regions (e.g., SEPO), the
319 differences between heavy and light precipitation regions are well distinguishable.

320

321 In the precipitation frequency distribution, many models show a bimodal distribution in the
322 heavy precipitating tropical ocean region (Fig. 6b) but not in the light precipitating
323 subtropical ocean region (Fig. 6e) or the heavy precipitating mid-latitude land region (Fig.
324 6h). The bimodal frequency distribution is a commonly found in models and is seemingly
325 independent of resolution (e.g., Lin et al. 2013; Kooperman et al. 2018; Chen et al. 2021;
326 Ma et al. 2022; Martinez-Villalobos et al. 2022; Ahn et al. 2023). Ma et al. (2022)
327 compared the frequency distributions in AMIP and HighResMIP (High Resolution Model
328 Intercomparison Project, Haarsma et al. 2016) from CMIP6 and DYAMOND (DYnamics
329 of the Atmospheric general circulation Modeled On Non-hydrostatic Domains, Satoh et
330 al. 2019; Stevens et al. 2019) models, where they showed that the bimodal frequency
331 distribution appears in many AMIP (~100km), HighResMIP (~50km), and even
332 DYAMOND (~4km) models. Ahn et al. (2023) further compared between DYAMOND
333 model simulations with and without a convective parameterization and showed that most
334 DYAMOND model simulations exhibiting the bimodal distribution use a convective
335 parameterization. ERA5 reanalysis also shows a bimodal frequency distribution (Fig. 6b),
336 which is not surprising considering that the reproduced precipitation in ERA5 heavily
337 depends on the model, thus exhibits this common model behavior. Because of the heavy
338 reliance on model physics to generate its precipitation (as opposed to fields like wind, for
339 which observations are directly assimilated), in this study we do not include ERA5
340 precipitation among the observational products used for model evaluation.

341

342 Based on the precipitation amount, frequency, and cumulative amount fraction curves,
343 we calculate 10 metrics (Amount peak, Amount P10, Amount P90, Frequency peak,
344 Frequency P10, Frequency P90, Unevenness, FracPRdays, SDII, and Perkins score) as
345 described in Section 3. Figure 7 shows the metrics with the modified IPCC AR6 climate
346 reference regions for satellite-based observations (black), ERA5 (gray), CMIP5 (blue),
347 and CMIP6 (red) models. The metric values vary widely across regions, especially in
348 Amount peak, Frequency peak, Unevenness, FracPRdays, and SDII, demonstrating the
349 additional detail provided by regional-scale precipitation-distribution metrics. In terms of
350 the metrics based on the amount distribution (Fig. 7a-c), many models tend to simulate
351 an Amount peak that is too light, an Amount P10 that is too high, and an Amount P90 that
352 is too low compared to the observations, moreso in oceanic regions (regions 47-62) than
353 in land regions. Similarly for the metrics based on the frequency distribution (Fig. 7d-f),
354 many models show light Frequency peaks, overestimated Frequency P10, and
355 underestimated Frequency P90 compared to observations. The similarity between
356 frequency distribution curves (i.e., Perkins score) is higher in land regions than in ocean
357 regions. Also, many models overestimate Unevenness and FracPRdays and
358 underestimate SDII. These results indicate that overall, models simulate more frequent
359 weak precipitation and less heavy precipitation compared to the observations, consistent
360 with many previous studies (e.g., Dai 2006; Pendergrass and Hartmann 2014; Trenberth
361 et al. 2017; Chen et al. 2021; Ma et al. 2022).

362

363 As expected from previous work, observations disagree substantially in some regions
364 (e.g., polar and high latitude regions) and/or for some metrics (e.g., Amount P90,

365 Frequency P90). In some cases the observational spread is much larger than that of the
366 models. We examine the observational discrepancy or spread by the ratio between the
367 standard deviation of the five satellite-based observations (IMERG, TRMM, CMORPH,
368 GPCP, PERSIANN) and the standard deviation of all CMIP 5 and 6 models (Fig. 8). The
369 standard deviation of observations is much larger near polar regions and high latitude
370 regions compared to the models' standard deviation for most metrics, as expected from
371 the orbital configurations of the most relevant satellite constellations for precipitation
372 (which exclude high latitudes). The Amount P90 and Frequency P90 metrics show the
373 largest observational discrepancy among the metrics, with standard deviations of 1.5 to
374 3 times larger over some high latitude regions and about 3-8 times larger over polar
375 regions in observations compared to the models. On the other hand, Unevenness,
376 FracPRdays, and Amount P10 show the least observational discrepancy – the models'
377 standard deviation is about 2-8 times larger than for observations over some tropical and
378 subtropical regions; nonetheless, the standard deviation among observations is larger
379 over most of the high latitude and polar regions. Model evaluation in the regions with large
380 disagreement among observational products remains a challenge. Note that the standard
381 deviation of five observations would be sensitive as there are outlier observations for
382 some regions and metrics (e.g., many ocean regions in Amount P90). Moreover,
383 observational uncertainties are rarely well quantified or understood, so agreements
384 among observational datasets may not always allow us to rule out common errors among
385 observations (e.g., for warm light precipitation over the subtropical ocean).

386

387 To attempt to account for discrepancies among observational datasets in the model
388 evaluation framework, we use two different approaches to evaluate model performance
389 with multiple observations, as described in Section 3.4. The first approach is to assess
390 the number of models that are within the observational range. Figure 9 shows the CMIP6
391 model evaluation with each metric, and the regions where the standard deviation among
392 observations is larger than among models are stippled gray to avoid them from the model
393 performance evaluation. In Amount peak, some subtropical regions (e.g., ARP, EAS,
394 NEPO, CAU, and WSAF) show relatively good model performance (more than 70% of
395 models fall in the observational range), while some tropical and subtropical (e.g., PITCZ,
396 AITCZ, and SEPO) and polar (e.g., RAR, EAN, and WAN) regions show poor model
397 performance (less than 30% of models fall in observational range). For Amount P10,
398 many regions are poorly captured by the simulations, except for some subtropical land
399 regions (e.g., EAS, NCA, CAU, and WSAF). In Amount P90, most regions are uncertain
400 (i.e., the standard deviation among observations is larger than among models) making it
401 difficult to evaluate model performance, while some tropical regions near the Indo-Pacific
402 warmpool (EIO, SEA, NWPO, and NAU) exhibit very good model performance (more than
403 90% of models fall in observational range). In the Frequency metrics (peak, P10, and
404 P90), more regions are difficult to evaluate model performance than in Amount metrics,
405 while in some tropical and subtropical regions (e.g., PITCZ, SWPO, NWPO, SEA, SAO,
406 and NES) model performance is good. However, good model performance could
407 alternatively arise from a large observational range (see Fig. 7). Unevenness,
408 FracPRdays, SDII, and Perkins score have a smaller fraction of models within the
409 observational range in tropical regions than the Amount and Frequency metrics. In

410 particular, fewer than 10% of CMIP6 models fall within the observational range for
411 Unevenness and FracPRdays over some tropical oceanic regions (e.g., PITCZ, NEPO,
412 SEPO, AITCZ, NEAO, SAO, and SIO).

413

414 Examining the fraction of CMIP5 models falling within the range of observations, CMIP5
415 models have a spatial pattern of model performance similar to that of CMIP6 models (see
416 Fig. S2 in supplement), and the improvement from CMIP5 to CMIP6 seems subtle. We
417 quantitatively assess the improvement from CMIP5 to CMIP6 by subtracting the
418 percentage of CMIP5 from CMIP6 models falling within the range of observations (Fig.
419 10). For some metrics (e.g., Amount peak, Amount and Frequency P10, and Amount and
420 Frequency P90) and for some tropical and subtropical regions (e.g., SEA, EAS, SAS,
421 ARP, and SAH), improvement is apparent. Compared to CMIP5, 5-25% more CMIP6
422 models fall in the observational range in these regions. However, for the other metrics
423 (e.g., Frequency peak, FracPRdays, SDII, Perkins score), CMIP6 models perform
424 somewhat worse. Over some tropical and subtropical oceanic regions (e.g., PITCZ,
425 NEPO, AITCZ, and NEAO), 5-25% more CMIP6 than CMIP5 models are out of the
426 observational range. This result is from all available CMIP5 and CMIP6 models, so it may
427 reflect the fact that some models are participated in only CMIP5 or CMIP6, but not both
428 (see Table 2). To isolate improvements that may have occurred between successive
429 generations of the same models, we also compared only the models that participated in
430 both CMIP5 and CMIP6 (see Fig. S3). Overall, the spatial characteristics of the
431 improvement/degradation in CMIP6 from CMIP5 is consistent, while more degradation is

432 apparent when we compare this subset of models, especially over the tropical oceanic
433 regions (e.g., PITCZ, AITCZ, NWPO, and SEPO).

434

435 The second approach to account for discrepancies among observations in model
436 performance evaluation is to count the number of models that are lower or higher than all
437 satellite-based observations for each metric and each region. Figure 11 shows the spatial
438 patterns of the model performance evaluation with each metric for CMIP6 models.
439 Underestimation is indicated by a negative sign, while overestimation is indicated by a
440 positive sign via the formulation described in Section 3.4. Amount peak is overall
441 underestimated in most regions, indicating the amount distributions in most CMIP6
442 models are shifted to lighter precipitation compared to observations. In many regions,
443 more than 50% of the CMIP6 models underestimate Amount peak. In particular, over
444 many tropical and southern hemisphere ocean regions (e.g., PITCZ, AITCZ, EIO, SEPO,
445 SAO, and SOO), more than 70% of the models underestimate the Amount peak. The
446 underestimation of Amount peak is accompanied by overestimation of Amount P10 and
447 underestimation of Amount P90. More than 70% of CMIP6 models overestimate Amount
448 P10 in many oceanic regions; especially in the southern and northern Pacific and Atlantic,
449 the southern Indian Ocean, and Southern Ocean more than 90% of the models
450 overestimate the observed Amount P10. For Amount P90, it appears that many models
451 fall within the observational range; however, observational range in Amount P90 (green
452 boxes in Fig. 7c) is large and driven primarily by just one observational dataset (IMERG),
453 especially in ocean regions.

454

455 For the frequency-based metrics (i.e., peak, P10, and P90; Figs. 11d-f), CMIP6 models
456 show similar bias characteristics to Amount metrics (Figs. 11a-c), although performance
457 is better than for Amount metrics. Over some tropical (e.g., NWPO, PITCZ, and SWPO)
458 and Eurasia (e.g., EEU, WSB, and ESB) regions, less than 10% of models fall outside of
459 the observed range. Unevenness and FracPRdays are severely overestimated in models.
460 More than 90% of models overestimate the observed Unevenness (Fig. 11g) and
461 FracPRdays (Fig. 11h) globally, especially over oceanic regions, consistent with
462 Pendergrass and Knutti (2018). SDII is underestimated in many regions globally,
463 especially in some heavily-precipitating regions (e.g., PITCZ, AITCZ, EIO, SEA, NPO,
464 NAO, SWPO, and SOO). For the Perkins score, model simulations have poorer
465 performance in the tropics than in the mid-latitudes and polar regions. Performance by
466 these various metrics is generally consistent with the often-blamed too-frequent light
467 precipitation and too rare heavy precipitation in simulations.

468

469 The characteristics of CMIP5 compared to CMIP6 simulations (Fig. S4) show little
470 indication of improvement. Here we quantitatively evaluate the improvement in CMIP6
471 from CMIP5 for each metric and region. Figure 12 shows the difference between CMIP5
472 and CMIP6 in terms of the percentage of models that under- or over-estimate each metric.
473 In mid-latitudes, there appears to have been an improvement in performance, however in
474 the tropics, there appears to be more degradation. Over some heavily-precipitating
475 tropical regions (e.g., PITCZ, AITCZ, EIO, and NWPO), 10-25% more models in CMIP6
476 than in CMIP5 overestimate Amount P10, Unevenness, and FracPRdays and
477 underestimate/underperform on Amount peak, SDII, and Perkins score. This indicates

478 that CMIP6 models simulate more frequent light precipitation and less frequent heavy
479 precipitation over the heavily-precipitating tropical regions. Over some mid-latitude land
480 regions (e.g., EAS, ESB, RFE, and ENA), on the other hand, 5-20% more models in
481 CMIP6 than in CMIP5 simulate precipitation distributions close to observations (i.e., less
482 light precipitation and more heavy precipitation). To evaluate the improvement between
483 model generation, we also compare only the models that participated in both CMIP5 and
484 CMIP6 (Fig. S5) rather than all available CMIP5 and CMIP6 models. For the subset of
485 models participating in both generations, the improvement characteristics are similar for
486 all models, although more degradation is exhibited over some tropical oceanic regions
487 (e.g., PITCZ, NWPO, and SWPO). This also indicates that some models newly
488 participating in CMIP6, and not in the CMIP5, have higher than average performance.

489

490 4.3. Correlation between metrics

491 Each precipitation distribution metric implemented in this study is chosen to target
492 different aspects of the distribution of precipitation. To the extent that precipitation
493 probability distributions are governed by a small number of key parameters (as argued by
494 Martinez-Villalobos and Neelin 2019), we should expect additional metrics to be highly
495 correlated. Figure 13 shows the global weighted average of correlation coefficients
496 between the precipitation distribution metrics across CMIP5 and CMIP6 models. Higher
497 correlation coefficients are found to be between Amount P90 and Frequency P90 (0.98)
498 and between Amount P10 and Frequency P10 (0.67). This is expected because the
499 amount and frequency distributions differ only by a factor of the precipitation rate (e.g.,
500 Pendergrass and Hartmann 2014). Another higher correlation coefficient is between

501 Unevenness and FracPRdays (0.77), indicating that the number of the heaviest
502 precipitating days for half of annual precipitation and the total number of annual
503 precipitating days are related. Amount and Frequency peak metrics are negatively
504 correlated to P10 metrics and positively correlated to P90 metrics, but the correlation
505 coefficients are not very high (lower than 0.62). This is because the peak metrics focus
506 on typical precipitation, rather than the light and heavy ends of the distribution that are
507 the focus of P10 and P90 metrics. SDII is more negatively correlated with Amount P10 (-
508 0.67) and positively correlated with Amount peak (0.61) and less so with Amount P90
509 (0.48), implying that SDII is mainly influenced by weak precipitation amounts rather than
510 heavy precipitation amounts. The Perkins score shows relatively high negative correlation
511 with Unevenness (-0.62), FracPRdays (-0.59), and Amount P10 (-0.59). This indicates
512 that the discrepancy between the observed and modeled frequency distributions is partly
513 associated with the overestimated light precipitation in models. The correlation
514 coefficients between the metrics other than those discussed above are lower than 0.6.
515 While there is some redundant information within the collection of metrics included in our
516 framework, we retain all metrics so that others can select an appropriate subset for their
517 own application. This also preserves the ability to readily identify outlier behavior of an
518 individual model across a wide range of regions and statistics.

519

520 4.4. Influence of spatial resolution on metrics

521 Many metrics for the precipitation distribution are sensitive to the spatial resolution of
522 the underlying data (e.g., Pendergrass and Knutti 2018; Chen and Dai 2019). Figure 14
523 shows how our results (which are all based on data at 2° resolution) are impacted if we

524 calculate the metrics from data coarsened to 4° grid instead. As expected, there is clearly
525 some sensitivity to the spatial scale at which our precipitation distribution metrics are
526 computed, but the correlation among datasets (both models and observations) between
527 the two resolutions is very high, indicating that evaluations at either resolution should be
528 consistent. At the coarser resolution, Amount peak and SDII are consistently smaller (as
529 expected); Amount P10 and Frequency P10 tend to be smaller as well. Meanwhile,
530 Unevenness and FracPRdays are consistently large (as expected); Amount P90,
531 Frequency P90, and Perkins score are generally larger as well. Chen and Dai (2019)
532 discussed a grid aggregation effect that is associated with the increased probability of
533 precipitation as the horizontal resolution becomes coarser. This effect is clearly evident
534 with increased Unevenness (Fig. 14g), FracPRdays (Fig. 14h), and decreased SDII (Fig.
535 14i) in coarser resolution. However, despite these differences, the relative model
536 performance is not very sensitive to the spatial scale at which we apply our analysis. The
537 correlation coefficients between results based on all data interpolated to 2° or 4°
538 horizontal resolutions are above 0.9 for all of our distribution metrics. Conclusions on
539 model performance are relatively insensitive to the target resolution.

540

541

542 **5. Discussion**

543 Analyzing the distribution of precipitation intensity lags behind temperature and even
544 mean precipitation. Challenges include choosing appropriate metrics and analysis
545 resolution to characterize this highly non-gaussian variable and interpreting model skills
546 in the face of substantial observational uncertainty. Comparing results derived at 2° and

547 4° horizontal resolution for CMIP class models, we find that the quantitative changes in
548 assessed performance are highly consistent across models and consequently have little
549 impact on our conclusions. More work is needed to determine how suitable this collection
550 of metrics may be for evaluating models with substantially higher resolutions (e.g.,
551 HighResMIP, Haarsma et al. 2016). We note that more complex measures have been
552 designed to be scale independent (e.g., Martinez-Villalobos and Neelin 2019; Martinez-
553 Villalobos et al. 2022), and these may become increasingly important with continued
554 interest in models developed at substantially higher resolution.

555

556 Several recent studies suggest that the IMERG represents a substantial advancement
557 over TRMM and likely the others (e.g., Wei et al. 2017; Khodadoust Siuki et al. 2017;
558 Zhang et al. 2018), thus we rely on IMERG as the default in much of our analysis.
559 However, we do not entirely discount the other products because the discrepancy
560 between them provides a measure of uncertainty in the satellite-based estimates of
561 precipitation. Our use of the minimum to maximum range of multiple observational
562 products is indicative of their discrepancy, but not their uncertainty, and thus is a limitation
563 of the current work and challenge that we hope will be addressed in the future.

564

565 The common model biases identified in this study are mainly associated with the
566 overestimated light precipitation and underestimated heavy precipitation. These biases
567 persist from deficiencies identified in earlier generation models (e.g., Dai 2006), and as
568 shown in this study there has been little improvement. One reason may be that these key
569 characteristics of precipitation are not commonly considered in the model development

570 process. Enabling modelers to more readily objectively evaluate simulated precipitation
571 distributions could perhaps serve as a guide to improvement. The current study aims to
572 provide a framework for objective evaluation of simulated precipitation distributions at
573 regional scales.

574

575 Imperfect convective parameterizations are a possible cause of the common model
576 biases in precipitation distributions (e.g., Lin et al. 2013; Kooperman et al. 2018; Ahn et
577 al. 2018; Chen and Dai 2019; Chen et al. 2021; Martinez-Villalobos et al. 2022). Many
578 convective parameterizations tend to produce too frequent and light precipitation, the so-
579 called “drizzling” bias (e.g., Dai 2006; Trenberth et al. 2017; Chen et al. 2021; Ma et al.
580 2022), and it is likely due to a fact that the parameterized convection is more readily
581 triggered than that in the nature (e.g., Lin et al. 2013; Chen et al. 2021). As model
582 horizontal resolution increases, grid-scale precipitation processes can lead to resolving
583 convective precipitation, as in so-called cloud resolving, storm resolving, or convective
584 permitting models. Ma et al. (2022) compare several storm resolving models in
585 DYAMOND to recent CMIP6 models with a convective parameterization and observe that
586 the simulated precipitation distributions are more realistic in the storm resolving models.
587 However, some of the storm resolving models still suffer from precipitation distribution
588 errors, including bimodality in the frequency distribution. Further studies are needed to
589 better understand the precipitation distribution biases in models.

590

591

592 **6. Conclusion**

593 We introduce a framework for regional scale evaluation of simulated precipitation
594 distributions with 62 climate reference regions and 10 precipitation distribution metrics
595 and apply it to evaluate the two most recent generations of climate model intercomparison
596 simulations (i.e., CMIP5 and CMIP6).

597

598 To facilitate the regional scale for evaluation, regions where precipitation characteristics
599 are relatively homogenous are identified. Our reference regions consist of existing IPCC
600 AR6 climate reference regions, with additional subdivisions based on homogeneity
601 analysis performed on precipitation distributions within each region. Our precipitation
602 clustering analysis reveals that the IPCC AR6 land regions are reasonably homogeneous
603 in precipitation character, while some ocean regions are relatively inhomogeneous,
604 including large portions of both heavy and light precipitating areas. To define more
605 homogeneous regions for the analysis of precipitation distributions, we have modified
606 some ocean regions to better fit the clustering results. Although the clustering regions are
607 obtained based on the IMERG annual precipitation, the improved homogeneity is fairly
608 consistent across different datasets (TRMM, CMORPH, GPCP, PERSIANN, and ERA5)
609 and seasons (MAM, JJA, SON, and DJF). Use of these more homogeneous regions
610 enables us to extract more robust quantitative information from the distributions in each
611 region.

612

613 To form the basis for evaluation within each region, we use a set of metrics that are well-
614 established and easy to interpret, aiming to extract key characteristics from the
615 distributions of precipitation frequency, amount, and cumulative fraction of precipitation

amount. We include the precipitation rate at the peak of the amount and frequency distributions (Kooperman et al., 2016; Pendergrass and Deser, 2017) and define several complementary metrics to measure the frequency and amount of precipitation under the 10th percentile (P10) and over the 90th percentile (P90). The distribution peak metrics assess whether the center of each distribution is shifted toward light or heavy precipitation, while the P10 and P90 metrics quantify the fraction of light and heavy precipitation in the distributions. The Perkins score is included to measure the similarity between the observed and modeled frequency distributions. Also, based on the cumulative fraction of precipitation amount, we implement the unevenness metric counting the number of wettest days for half of the annual precipitation (Pendergrass and Knutti 2018), the fraction of annual precipitating days above 1 mm/day, and the simple daily intensity index (Zhang et al. 2011).

We apply the framework of regional scale precipitation distribution benchmarking to all available realizations of 25 CMIP5 and 41 CMIP6 models and 5 satellite-based precipitation products (IMERG, TRMM, CMORPH, GPCP, PERSIANN). The observational discrepancy is substantially larger compared to the models' spread for some regions, especially for mid-latitude and polar regions and for some metrics such as Amount P90 and Frequency P90. We use two approaches to account for observational discrepancy in the model evaluation. One is based on the number of models within the observational range, and another is the number of models below/above all observations. In this way, we can draw some conclusions on the overall performance in the CMIP ensemble even in the presence of observations that may substantially disagree in certain

639 regions. Many CMIP5 and CMIP6 models underestimate the Amount and Frequency
640 peaks and overestimate Amount and Frequency P10 compared to observations,
641 especially in many mid-latitude regions where more than 50% of the models are out of
642 the observational range. This indicates that models produce too frequent light
643 precipitation, a bias that is also revealed by the overestimated FracPRdays and the
644 underestimated SDII. Unevenness is the metric that models simulate the worst – in many
645 regions more than 70-90% of the models are out of the observational range. Clear
646 changes in performance between CMIP5 and CMIP6 are limited. Considering all metrics,
647 the CMIP6 models show improvement in some mid-latitude regions, but in a few tropical
648 regions the CMIP6 models actually show performance degradation.

649

650 The framework presented in this study is intended to be a useful resource for model
651 evaluation analysts and developers working towards improved performance for a wide
652 range of precipitation characteristics. Basing the regions in part on homogeneous
653 precipitation characteristics can facilitate identification of the processes responsible for
654 model errors as heavy precipitating regions are generally dominated by convective
655 precipitation, while the moderate and light precipitation regions are mainly governed by
656 stratiform precipitation processes. Although the framework presented herein has been
657 demonstrated with regional scale evaluation benchmarking, it can be applicable for
658 benchmarking at larger scales and homogeneous precipitation regions.

659

660 **Code Availability**

661 The benchmarking framework for precipitation distributions established in this study is
662 available via the PCMDI Metrics Package (PMP,
663 https://github.com/PCMDI/pcmdi_metrics, DOI: [10.5281/zenodo.7231033](https://doi.org/10.5281/zenodo.7231033)). This
664 framework provides three tiers of area averaged outputs for i) large scale domain (Tropics
665 and Extratropics with separated land and ocean) commonly used in the PMP, ii) large
666 scale domain with clustered precipitation characteristics (Tropics and Extratropics with
667 separated land and ocean, and separated heavy, moderate, and light precipitation
668 regions), and iii) modified IPCC AR6 regions shown in this paper.

669

670

671 **Data Availability**

672 All of the data used in this study are publicly available. The satellite-based precipitation
673 products used in this study (IMERG, TRMM, CMORPH, GPCP, and PERSIANN) and
674 ERA5 precipitation product are available on the Obs4MIPs at <https://esgf-node.llnl.gov/projects/obs4mips/>. The CMIP data is available on the ESGF at <https://esgf-node.llnl.gov/projects/esgf-llnl>. The statistics generated from this benchmarking
675 framework and the interactive plots with access to the underlying diagnostics were made
676 available on the PCMDI Simulation Summaries at
677 <https://pcmdi.llnl.gov/research/metrics/precip/>.

680

681

682 **Author contribution**

683 PG and AP designed the initial idea of the precipitation benchmarking framework. MA,
684 PU, PG, and JL advanced the idea and developed the framework. MA performed
685 analysis. MA, JL, and AO implemented the framework code into the PCMDI metrics
686 package. MA prepared the manuscript with contributions from all co-authors.

687

688

689 **Competing interests**

690 The authors declare that they have no conflict of interest.

691

692

693 **Disclaimer**

694 This document was prepared as an account of work sponsored by an agency of the U.S.
695 government. Neither the U.S. government nor Lawrence Livermore National Security,
696 LLC, nor any of their employees makes any warranty, expressed or implied, or assumes
697 any legal liability or responsibility for the accuracy, completeness, or usefulness of any
698 information, apparatus, product, or process disclosed, or represents that its use would
699 not infringe privately owned rights. Reference herein to any specific commercial product,
700 process, or service by trade name, trademark, manufacturer, or otherwise does not
701 necessarily constitute or imply its endorsement, recommendation, or favoring by the U.S.
702 government or Lawrence Livermore National Security, LLC. The views and opinions of
703 authors expressed herein do not necessarily state or reflect those of the U.S. government
704 or Lawrence Livermore National Security, LLC, and shall not be used for advertising or
705 product endorsement purposes.

706

707

708 **Acknowledgements**

709 This work was performed under the auspices of the U.S. Department of Energy by
710 Lawrence Livermore National Laboratory under Contract DE-AC52-07NA27344. The
711 efforts of the authors were supported by the Regional and Global Model Analysis (RGMA)
712 program of the United States Department of Energy's Office of Science, including under
713 Award Number DE-SC0022070 and National Science Foundation (NSF) IA 1947282.

714 This work was also partially supported by the National Center for Atmospheric Research
715 (NCAR), which is a major facility sponsored by the NSF under Cooperative Agreement
716 No. 1852977. We acknowledge the World Climate Research Programme's Working
717 Group on Coupled Modeling, which is responsible for CMIP, and we thank the climate
718 modeling groups for producing and making available their model output, the Earth System
719 Grid Federation (ESGF) for archiving the output and providing access, and the multiple
720 funding agencies who support CMIP and ESGF. The U.S. Department of Energy's
721 Program for Climate Model Diagnosis and Intercomparison (PCMDI) provides
722 coordinating support and led development of software infrastructure for CMIP.

723

724 **References**

725 Abramowitz, G. (2012). Towards a public, standardized, diagnostic benchmarking
726 system for land surface models. *Geoscientific Model Development*, 5(3), 819–
727 827. <https://doi.org/10.5194/gmd-5-819-2012>.

728 Ahn, M., and I. Kang, 2018: A practical approach to scale-adaptive deep convection
729 in a GCM by controlling the cumulus base mass flux. *npj Clim. Atmos. Sci.*, 1,
730 13, <https://doi.org/10.1038/s41612-018-0021-0>.

731 Ahn, M.-S., P. A. Ullrich, J. Lee, P. J. Gleckler, H.-Y. Ma, C. R. Terai, P. A.
732 Bogenschutz, and A. C. Ordonez, 2023: Bimodality in Simulated Precipitation
733 Frequency Distributions and Its Relationship with Convective Parameterizations.
734 *npj Climate and Atmospheric Science*, submitted.

735 Ahn, M.-S., P. J. Gleckler, J. Lee, A. G. Pendergrass, and C. Jakob, 2022:
736 Benchmarking Simulated Precipitation Variability Amplitude across Time
737 Scales. *J. Clim.*, 35, 3173–3196, <https://doi.org/10.1175/JCLI-D-21-0542.1>.

738 Ashouri, H., K. L. Hsu, S. Sorooshian, D. K. Braithwaite, K. R. Knapp, L. D. Cecil, B.
739 R. Nelson, and O. P. Prat, 2015: PERSIANN-CDR: Daily precipitation climate
740 data record from multisatellite observations for hydrological and climate studies.
741 *Bull. Am. Meteorol. Soc.*, 96, 69–83, <https://doi.org/10.1175/BAMS-D-13-00068.1>.

743 Chakravarti, I. M., R. G. Laha, and J. Roy, 1967: Handbook of Methods of Applied
744 Statistics, Volume I: Techniques of Computation, Descriptive Methods, and
745 Statistical Inference. *John Wiley Sons*, 392–394.

746 Chen, D., and A. Dai, 2019: Precipitation Characteristics in the Community
747 Atmosphere Model and Their Dependence on Model Physics and Resolution. *J.*
748 *Adv. Model. Earth Syst.*, **11**, 2352–2374,
749 <https://doi.org/10.1029/2018MS001536>.

750 Chen, D., A. Dai, and A. Hall, 2021: The Convective-To-Total Precipitation Ratio and
751 the “Drizzling” Bias in Climate Models. *J. Geophys. Res. Atmos.*, **126**, 1–17,
752 <https://doi.org/10.1029/2020JD034198>.

753 Covey, C., Gleckler, P. J., Doutriaux, C., Williams, D. N., Dai, A., Fasullo, J.,
754 Trenberth, K., & Berg, A. (2016). Metrics for the Diurnal Cycle of Precipitation:
755 Toward Routine Benchmarks for Climate Models. *Journal of Climate*, **29**(12),
756 4461–4471. <https://doi.org/10.1175/JCLI-D-15-0664.1>

757 Dai, A., 2006: Precipitation characteristics in eighteen coupled climate models. *J.*
758 *Clim.*, **19**, 4605–4630, <https://doi.org/10.1175/JCLI3884.1>.

759 Eyring, V., S. Bony, G. A. Meehl, C. A. Senior, B. Stevens, R. J. Stouffer, and K. E.
760 Taylor, 2016: Overview of the Coupled Model Intercomparison Project Phase 6
761 (CMIP6) experimental design and organization. *Geosci. Model Dev.*, **9**, 1937–
762 1958, <https://doi.org/10.5194/gmd-9-1937-2016>.

763 Fiedler, S., and Coauthors, 2020: Simulated Tropical Precipitation Assessed across
764 Three Major Phases of the Coupled Model Intercomparison Project (CMIP).
765 *Mon. Weather Rev.*, **148**, 3653–3680, <https://doi.org/10.1175/MWR-D-19-0404.1>.

767 Gleckler, P., C. Doutriaux, P. Durack, K. Taylor, Y. Zhang, D. Williams, E. Mason,
768 and J. Servonnat, 2016: A More Powerful Reality Test for Climate Models. *Eos*
769 (*Washington. DC.*), **97**, 20–24, <https://doi.org/10.1029/2016EO051663>.

770 Gleckler, P. J., K. E. Taylor, and C. Doutriaux, 2008: Performance metrics for climate
771 models. *J. Geophys. Res. Atmos.*, **113**, 1–20,
772 <https://doi.org/10.1029/2007JD008972>.

773 Hersbach, H., and Coauthors, 2020: The ERA5 global reanalysis. *Q. J. R. Meteorol. Soc.*, **146**, 1999–2049, <https://doi.org/10.1002/qj.3803>.

775 Huffman, G. J., and Coauthors, 2007: The TRMM Multisatellite Precipitation Analysis
776 (TMPA): Quasi-Global, Multiyear, Combined-Sensor Precipitation Estimates at
777 Fine Scales. *J. Hydrometeorol.*, **8**, 38–55, <https://doi.org/10.1175/JHM560.1>.

778 Huffman, G. J., and Coauthors, 2020: Integrated Multi-satellite Retrievals for the
779 Global Precipitation Measurement (GPM) Mission (IMERG). *Advances in Global
780 Change Research*, Vol. 67 of, 343–353.

781 Huffman, G. J., R. F. Adler, M. M. Morrissey, D. T. Bolvin, S. Curtis, R. Joyce, B.
782 McGavock, and J. Susskind, 2001: Global Precipitation at One-Degree Daily

783 Resolution from Multisatellite Observations. *J. Hydrometeorol.*, **2**, 36–50,
784 [https://doi.org/10.1175/1525-7541\(2001\)002<0036:GPAODD>2.0.CO;2](https://doi.org/10.1175/1525-7541(2001)002<0036:GPAODD>2.0.CO;2).

785 Iturbide, M., and Coauthors, 2020: An update of IPCC climate reference regions for
786 subcontinental analysis of climate model data: definition and aggregated
787 datasets. *Earth Syst. Sci. Data*, **12**, 2959–2970, <https://doi.org/10.5194/essd-12-2959-2020>.

789 Khodadoust Siuki, S., B. Saghafian, and S. Moazami, 2017: Comprehensive
790 evaluation of 3-hourly TRMM and half-hourly GPM-IMERG satellite precipitation
791 products. *Int. J. Remote Sens.*, **38**, 558–571,
792 <https://doi.org/10.1080/01431161.2016.1268735>.

793 Kim, S., A. Sharma, C. Wasko, and R. Nathan, 2022: Linking Total Precipitable Water
794 to Precipitation Extremes Globally. *Earth's Futur.*, **10**,
795 <https://doi.org/10.1029/2021EF002473>.

796 Kooperman, G. J., M. S. Pritchard, M. A. Burt, M. D. Branson, and D. A. Randall,
797 2016: Robust effects of cloud superparameterization on simulated daily rainfall
798 intensity statistics across multiple versions of the Community Earth System
799 Model. *J. Adv. Model. Earth Syst.*, **8**, 140–165,
800 <https://doi.org/10.1002/2015MS000574>.

801 Kooperman, G. J., M. S. Pritchard, T. A. O'Brien, and B. W. Timmermans, 2018:
802 Rainfall From Resolved Rather Than Parameterized Processes Better
803 Represents the Present-Day and Climate Change Response of Moderate Rates

804 in the Community Atmosphere Model. *J. Adv. Model. Earth Syst.*, **10**, 971–988,
805 <https://doi.org/10.1002/2017MS001188>.

806 Leung, L. R., and Coauthors, 2022: Exploratory Precipitation Metrics: Spatiotemporal
807 Characteristics, Process-Oriented, and Phenomena-Based. *J. Clim.*, **35**, 3659–
808 3686, <https://doi.org/10.1175/JCLI-D-21-0590.1>.

809 Lin, Y., M. Zhao, Y. Ming, J.-C. Golaz, L. J. Donner, S. A. Klein, V. Ramaswamy, and
810 S. Xie, 2013: Precipitation Partitioning, Tropical Clouds, and Intraseasonal
811 Variability in GFDL AM2. *J. Clim.*, **26**, 5453–5466, <https://doi.org/10.1175/JCLI-D-12-00442.1>.

813 Ma, H., S. A. Klein, J. Lee, M. Ahn, C. Tao, and P. J. Gleckler, 2022: Superior Daily
814 and Sub-Daily Precipitation Statistics for Intense and Long-Lived Storms in
815 Global Storm-Resolving Models. *Geophys. Res. Lett.*, **49**,
816 <https://doi.org/10.1029/2021GL096759>.

817 MacQueen, J. B., 1967: Some methods for classification and analysis of multivariate
818 observations. *Berkeley Symp. Math. Stat. Probab.*, **VOL. 5.1**, 281–297.

819 Martinez-Villalobos, C., and J. D. Neelin, 2019: Why Do Precipitation Intensities Tend
820 to Follow Gamma Distributions? *J. Atmos. Sci.*, **76**, 3611–3631,
821 <https://doi.org/10.1175/JAS-D-18-0343.1>.

822 Martinez-Villalobos, C., J. D. Neelin, and A. G. Pendergrass, 2022: Metrics for
823 Evaluating CMIP6 Representation of Daily Precipitation Probability Distributions.
824 *J. Clim.*, 1–79, <https://doi.org/10.1175/JCLI-D-21-0617.1>.

825 Meehl, G. A., C. Covey, B. McAvaney, M. Latif, and R. J. Stouffer, 2005: Overview
826 of the Coupled Model Intercomparison Project. *Bull. Am. Meteorol. Soc.*, **86**, 89–
827 96, <https://doi.org/10.1175/BAMS-86-1-89>.

828 Meehl, G. A., C. Covey, T. Delworth, M. Latif, B. McAvaney, J. F. B. Mitchell, R. J.
829 Stouffer, and K. E. Taylor, 2007: THE WCRP CMIP3 Multimodel Dataset: A New
830 Era in Climate Change Research. *Bull. Am. Meteorol. Soc.*, **88**, 1383–1394,
831 <https://doi.org/10.1175/BAMS-88-9-1383>.

832 Meehl, G. A., G. J. Boer, C. Covey, M. Latif, and R. J. Stouffer, 2000: The Coupled
833 Model Intercomparison Project (CMIP). *Bull. Am. Meteorol. Soc.*, **81**, 313–318,
834 [https://doi.org/10.1175/1520-0477\(2000\)081<0313:TCMIPC>2.3.CO;2](https://doi.org/10.1175/1520-0477(2000)081<0313:TCMIPC>2.3.CO;2).

835 Pendergrass, A. G., and C. Deser, 2017: Climatological Characteristics of Typical
836 Daily Precipitation. *J. Clim.*, **30**, 5985–6003, <https://doi.org/10.1175/JCLI-D-16-0684.1>.

838 Pendergrass, A. G., and D. L. Hartmann, 2014: Two Modes of Change of the
839 Distribution of Rain*. *J. Clim.*, **27**, 8357–8371, <https://doi.org/10.1175/JCLI-D-14-00182.1>.

841 Pendergrass, A. G., and R. Knutti, 2018: The Uneven Nature of Daily Precipitation
842 and Its Change. *Geophys. Res. Lett.*, **45**, 11,980–11,988,
843 <https://doi.org/10.1029/2018GL080298>.

844 Pendergrass, A. G., P. J. Gleckler, L. R. Leung, and C. Jakob, 2020: Benchmarking
845 Simulated Precipitation in Earth System Models. *Bull. Am. Meteorol. Soc.*, **101**,
846 E814–E816, <https://doi.org/10.1175/BAMS-D-19-0318.1>.

847 Perkins, S. E., A. J. Pitman, N. J. Holbrook, and J. McAneney, 2007: Evaluation of
848 the AR4 Climate Models' Simulated Daily Maximum Temperature, Minimum
849 Temperature, and Precipitation over Australia Using Probability Density
850 Functions. *J. Clim.*, **20**, 4356–4376, <https://doi.org/10.1175/JCLI4253.1>.

851 Roca, R., L. V. Alexander, G. Potter, M. Bador, R. Jucá, S. Contractor, M. G.
852 Bosilovich, and S. Cloché, 2019: FROGS: a daily $1^\circ \times 1^\circ$ gridded precipitation
853 database of rain gauge, satellite and reanalysis products. *Earth Syst. Sci. Data*,
854 **11**, 1017–1035, <https://doi.org/10.5194/essd-11-1017-2019>.

855 Stephens, M. A., 1974: EDF Statistics for Goodness of Fit and Some Comparisons.
856 *J. Am. Stat. Assoc.*, **69**, 730–737, <https://doi.org/10.2307/2286009>.

857 Sun, Y., S. Solomon, A. Dai, and R. W. Portmann, 2006: How Often Does It Rain? *J.*
858 *Clim.*, **19**, 916–934, <https://doi.org/10.1175/JCLI3672.1>.

859 Sun, Y., S. Solomon, A. Dai, and R. W. Portmann, 2007: How Often Will It Rain? *J.*
860 *Clim.*, **20**, 4801–4818, <https://doi.org/10.1175/JCLI4263.1>.

861 Swenson, L. M., and R. Grotjahn, 2019: Using Self-Organizing Maps to Identify
862 Coherent CONUS Precipitation Regions. *J. Clim.*, **32**, 7747–7761,
863 <https://doi.org/10.1175/JCLI-D-19-0352.1>.

883 Waliser, D., and Coauthors, 2020: Observations for Model Intercomparison Project
884 (Obs4MIPs): status for CMIP6. *Geosci. Model Dev.*, **13**, 2945–2958,
885 <https://doi.org/10.5194/gmd-13-2945-2020>.

886 Wehner, M., P. Gleckler, J. Lee, 2020: Characterization of long period return values
887 of extreme daily temperature and precipitation in the CMIP6 models: Part 1,
888 model evaluation. *Weather and Climate Extremes*, **30**, 100283, doi:
889 [10.1016/j.wace.2020.100283](https://doi.org/10.1016/j.wace.2020.100283).

890 Wei, G., H. Lü, W. T. Crow, Y. Zhu, J. Wang, and J. Su, 2017: Evaluation of Satellite-
891 Based Precipitation Products from IMERG V04A and V03D, CMORPH and
892 TMPA with Gauged Rainfall in Three Climatologic Zones in China. *Remote*
893 *Sens.*, **10**, 30, <https://doi.org/10.3390/rs10010030>.

894 Xie, P., R. Joyce, S. Wu, S. H. Yoo, Y. Yarosh, F. Sun, and R. Lin, 2017:
895 Reprocessed, bias-corrected CMORPH global high-resolution precipitation
896 estimates from 1998. *J. Hydrometeorol.*, **18**, 1617–1641,
897 <https://doi.org/10.1175/JHM-D-16-0168.1>.

898 Zhang, C., X. Chen, H. Shao, S. Chen, T. Liu, C. Chen, Q. Ding, and H. Du, 2018:
899 Evaluation and intercomparison of high-resolution satellite precipitation
900 estimates-GPM, TRMM, and CMORPH in the Tianshan Mountain Area. *Remote*
901 *Sens.*, **10**, <https://doi.org/10.3390/rs10101543>.

902 Zhang, X., L. Alexander, G. C. Hegerl, P. Jones, A. K. Tank, T. C. Peterson, B.
903 Trewin, and F. W. Zwiers, 2011: Indices for monitoring changes in extremes

904 based on daily temperature and precipitation data. *Wiley Interdiscip. Rev. Clim.*
905 *Chang.*, **2**, 851–870, <https://doi.org/10.1002/wcc.147>.

906 **Tables**

907

908

909

910 Table 1. Satellite-based and reanalysis precipitation products used in this study.

911

Product	Data source	Coverage		Resolution		Reference
		Domain	Period	Horizontal	Frequency	
IMERG	NASA Integrated Multi-satellitE Retrievals for GPM version 6 final run product	Global, while beyond 60°NS is incomplete	2000.6-present	0.1°	30 minutes	Huffman et al. (2020)
TRMM	NASA Tropical Rainfall Measuring Mission Multi-satellite Precipitation Analysis 3B42 version 7 product	50°S-50°N	1998.1-2019.12	0.25°	3 hours	Huffman et al. (2007)
CMORPH	NOAA Bias-corrected Climate Prediction Center Morphing technique product	60°S-60°N	1998.1-present	0.073°	30 minutes	Xie et al. (2017)
GPCP	NASA Global Precipitation Climatology Project 1DD version 1.3	Global, while beyond 40°NS is incomplete	1996.10-present	1°	1 day	Huffman et al. (2001)
PERSIANN	UC-IRVINE/CHRS Precipitation Estimation from Remotely Sensed Information using Artificial Neural Networks-Climate Data Record	60°S-60°N	1983.1-present	0.25°	1 day	Ashouri et al. (2015)
ERA5	ECMWF Integrated Forecasting System Cy41r2	Global	1950.1-present	0.25°	1 hour	Hersbach et al. (2020)

912

913

914

915

916

917

918

919

920

921

922

923

924

925
926
927
928
929
930

Table 2. CMIP5 and CMIP6 models used in this study and their horizontal resolution. The number in parentheses indicates the number of realizations used for each model. Note that the horizontal resolution information is obtained from the number of grids, and it may vary slightly if the grid interval is not linear.

Institute	CMIP5		CMIP6	
	Name	Horizontal resolution [lon x lat °]	Name	Horizontal resolution [lon x lat °]
CSIRO/BOM, Australia	ACCESS1-0 (1)	1.875 x 1.241	ACCESS-CM2 (7)	1.875 x 1.25
	ACCESS1-3 (2)	1.875 x 1.241	ACCESS-ESM1-5 (10)	1.875 x 1.241
BCC, China	BCC-CSM1-1 (3)	1.875 x 1.241	BCC-CSM2-MR (3)	1.125 x 1.125
	BCC-CSM1-1-M (3)	1.125 x 1.125	BCC-ESM1 (3)	2.812 x 2.812
BNU, China	BNU-ESM (1)	2.812 x 2.812	N/A	
CAMS, China	N/A		CAMS-CSM1-0 (3)	
CCCma, Canada	N/A		CanESM5 (7)	2.812 x 2.812
NCAR, USA	CCSM4 (6)	1.25 x 0.938	CESM2 (10)	1.25 x 0.938
			CESM2-FV2 (3)	2.5 x 1.875
			CESM2-WACCM (3)	1.25 x 0.938
			CESM2-WACCM-FV2 (3)	2.5 x 1.875
CMCC, Italy	CMCC-CM (3)	0.75 x 0.75	CMCC-CM2-HR4 (1)	1.25 x 0.938
			CMCC-CM2-SR5 (1)	1.25 x 0.938
CNRM-CERFACS, France		N/A	CNRM-CM6-1 (1)	1.406 x 1.406
			CNRM-CM6-1-HR (1)	0.5 x 0.5
			CNRM-ESM2-1 (1)	1.406 x 1.406
CSIRO-QCCCE, Australia	CSIRO-Mk3-6-0 (10)	1.875 x 1.875	N/A	
DOE, USA	N/A		E3SM-1-0 (3)	1.0 x 1.0
EC-Earth- Consortium, European Community	EC-Earth (1)	1.125 x 1.125	EC-Earth3 (6)	0.703 x 0.703
			EC-Earth3-AerChem (1)	0.703 x 0.703
			EC-Earth3-CC (5)	
			EC-Earth3-Veg (3)	0.703 x 0.703
IAP-CAS/THU, China	FGOALS-g2 (1)	2.812 x 3.0	FGOALS-f3-L (3)	1.0 x 1.0
	FGOALS-s2 (3)	2.812 x 1.667		
NOAA GFDL, USA	GFDL-CM3 (5)	2.5 x 2.0	GFDL-CM4 (1)	1.0 x 1.0
	GFDL-HIRAM-C180 (2)	0.625 x 0.5	GFDL-ESM4 (1)	1.0 x 1.0
	GFDL-HIRAM-C360 (1)	0.312 x 0.25		
NASA GISS, USA	GISS-E2-R (2)	2.5 x 2.0	N/A	
MOHC, UK	HadGEM2-A (1)	1.875 x 1.241	HadGEM3-GC31-LL (5)	1.875 x 1.25
			HadGEM3-GC31-MM (4)	0.833 x 0.556
			UKESM1-0-LL (1)	1.875 x 1.25
IITM, India	N/A		IITM-ESM (1)	1.875 x 1.915
INM, Russia	INMCM4 (1)	2.0 x 1.5	INM-CM4-8 (1)	2.0 x 1.5
			INM-CM5-0 (1)	2.0 x 1.5

IPSL, France	IPSL-CM5A-LR (6)	3.75 x 1.875	IPSL-CM6A-LR (22)	2.5 x 1.259
	IPSL-CM5A-MR (3)	2.5 x 1.259		
	IPSL-CM5B-LR (1)	3.75 x 1.875		
NIMS/KMA, Korea	N/A		KACE-1-0-G (1)	1.875 x 1.25
MIROC, Japan	MIROC5 (2)	1.406 x 1.406	MIROC6 (10)	1.406 x 1.406
			MIROC-ES2L (3)	2.812 x 2.812
MPI-M, Germany	MPI-ESM-MR (3)	1.875 x 1.875	MPI-ESM1-2-HAM (3)	1.875 x 1.875
			MPI-ESM1-2-HR (3)	0.938 x 0.938
			MPI-ESM1-2-LR (3)	1.875 x 1.875
MRI, Japan	MRI-AGCM3-2H (1)	0.562 x 0.562	MRI-ESM2-0 (3)	1.125 x 1.125
	MRI-AGCM3-2S (1)	0.188 x 0.188		
	MRI-CGCM3 (3)	1.125 x 1.125		
NCC, Norway	N/A		NorCPM1 (10)	2.5 x 1.875
			NorESM2-LM (2)	2.5 x 1.875
SNU, Korea	N/A		SAM0-UNICON (1)	1.25 x 0.938
AS-RCEC, Taiwan	N/A		TaiESM1 (1)	1.25 x 0.938

931

932

933

934

935

936

937

938

939

940

941

942

943

944

945

946

947

948

949

950

951

952

953

954

955

956
957
958

Table 3. Precipitation distribution metrics implemented in this study.

Metric [unit]	Definition	Objectives	Reference
Amount peak [mm/day]	Rain rate where the maximum rain amount occurs	Characterize typical daily precipitation amount	Pendergrass and Deser (2017)
Amount P10 [fraction]	Fraction of rain amount in lower 10 percentile of OBS amount	Measure the rain amount from light rainfall	
Amount P90 [fraction]	Fraction of rain amount in upper 90 percentile of OBS amount	Measure the rain amount from heavy rainfall	
Frequency peak [mm/day]	Rain rate where the maximum nonzero rain frequency occurs	Characterize typical daily precipitation frequency	Pendergrass and Deser (2017)
Frequency P10 [fraction]	Fraction of rain frequency in lower 10 percentile of OBS amount	Measure the frequency of light rainfall	
Frequency P90 [fraction]	Fraction of rain frequency in upper 90 percentile of OBS amount	Measure the frequency of heavy rainfall	
Unevenness [days]	Number of wettest days for that constitute half of annual precipitation	Measure uneven characteristic of daily precipitation	Pendergrass and Knutti (2018)
FracPRdays [fraction]	Number of precipitating days ($\geq 1\text{mm/day}$) divided by total days a year	Measure fraction of precipitating days a year	Updated from Zhang et al. (2011)
SDII [mm/day]	Annual total precipitation divided by the number of precipitating days ($\geq 1\text{mm/day}$)	Measure daily precipitation intensity	Zhang et al. (2011)
Perkins score [unitless between 0-1]	Sum of minimum values between two PDFs across all bins	Measure similarity between two PDFs	Perkins et al. (2007)

959
960
961
962
963
964

965
966
967
968

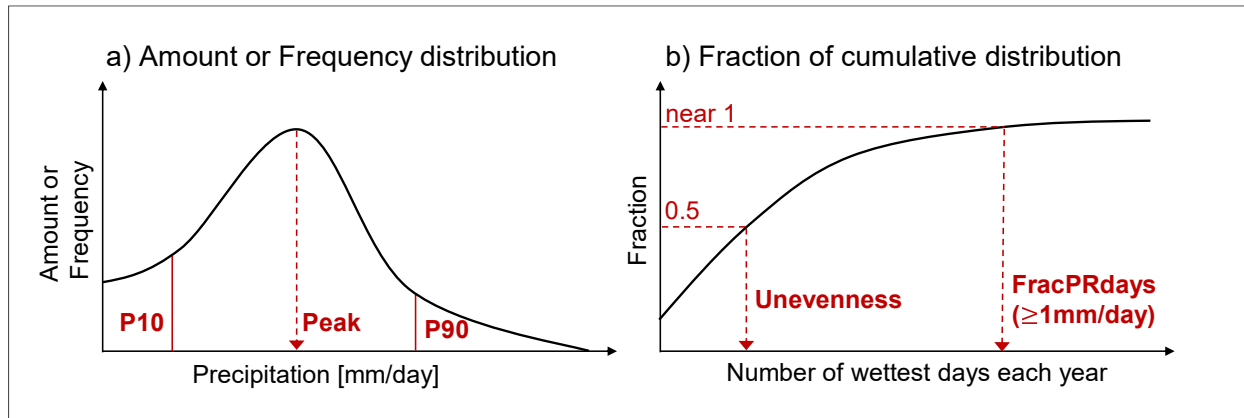
Table 4. List of climate reference regions used in this study. The new ocean regions defined in this study are highlighted in bold.

1	GIC	Greenland/Iceland	22	WAF	Western-Africa	43	SAU	S.Australia
2	NWN	N.W.North-America	23	CAF	Central-Africa	44	NZ	New-Zealand
3	NEN	N.E.North-America	24	NEAF	N.Eastern-Africa	45	EAN	E.Antarctica
4	WNA	W.North-America	25	SEAF	S.Eastern-Africa	46	WAN	W.Antarctica
5	CNA	C.North-America	26	WSAF	W.Southern-Africa	47	ARO	Arctic-Ocean
6	ENA	E.North-America	27	ESAF	E.Southern-Africa	48	ARS	Arabian-Sea
7	NCA	N.Central-America	28	MDG	Madagascar	49	BOB	Bay-of-Bengal
8	SCA	S.Central-America	29	RAR	Russian-Arctic	50	EIO	Equatorial-Indian-Ocean
9	CAR	Caribbean	30	WSB	W.Siberia	51	SIO	S.Indian-Ocean
10	NWS	N.W.South-America	31	ESB	E.Siberia	52	NPO	N.Pacific-Ocean
11	NSA	N.South-America	32	RFE	Russian-Far-East	53	NWP O	N.W.Pacific-Ocean
12	NES	N.E.South-America	33	WCA	W.C.Asia	54	NEPO	N.E.Pacific-Ocean
13	SAM	South-American-Monsoon	34	ECA	E.C.Asia	55	PITCZ	Pacific-ITCZ
14	SWS	S.W.South-America	35	TIB	Tibetan-Plateau	56	SWPO	S.W.Pacific-Ocean
15	SES	S.E.South-America	36	EAS	E.Asia	57	SEPO	S.E.Pacific-Ocean
16	SSA	S.South-America	37	ARP	Arabian-Peninsula	58	NAO	N.Atlantic-Ocean
17	NEU	N.Europe	38	SAS	S.Asia	59	NEAO	N.E.Atlantic-Ocean
18	WCE	West&Central-Europe	39	SEA	S.E.Asia	60	AITCZ	Atlantic-ITCZ
19	EEU	E.Europe	40	NAU	N.Australia	61	SAO	S.Atlantic-Ocean
20	MED	Mediterranean	41	CAU	C.Australia	62	SOO	Southern-Ocean
21	SAH	Sahara	42	EAU	E.Australia			

969

970 **Figures**

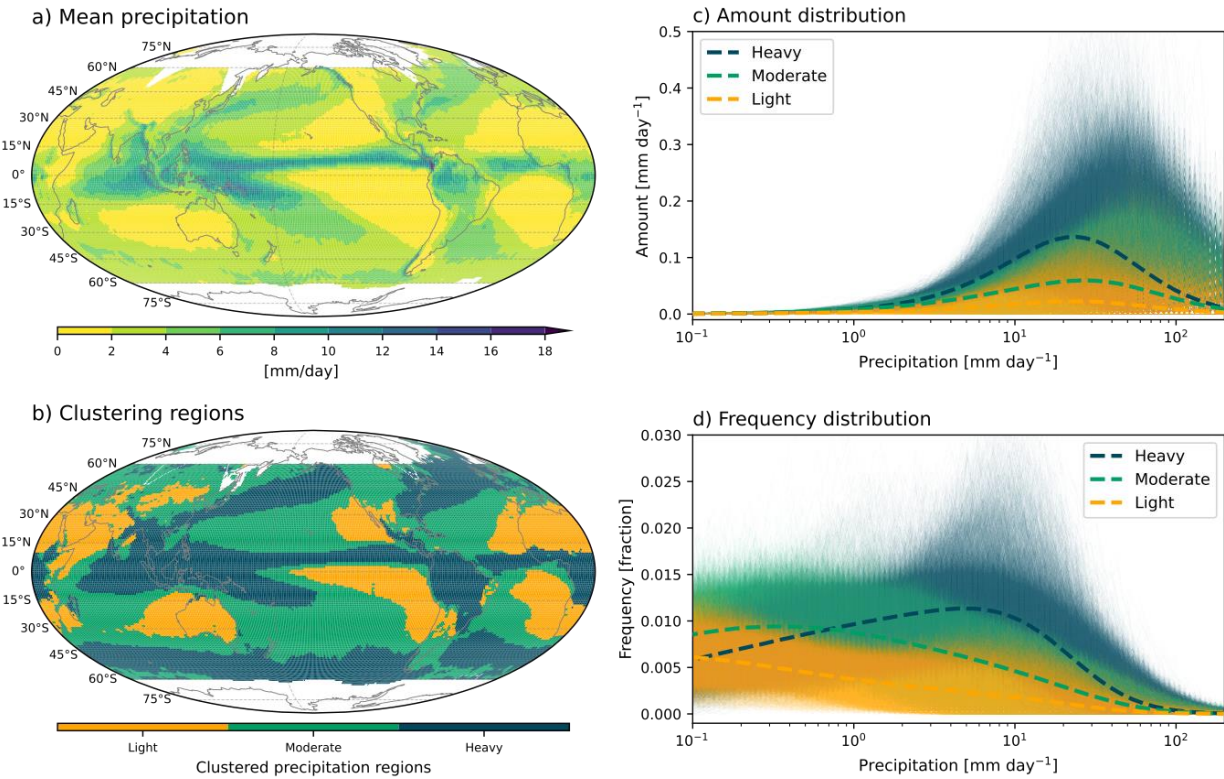
971
972
973
974
975
976



978
979 Figure 1. Schematics for precipitation distribution metrics. a) Amount or Frequency
980 distribution as a function of rain rate. Peak metric gauges the rain rate where the
981 maximum distribution occurs. P10 and P90 metrics respectively measure the fraction of
982 the distribution lower 10 percentile and upper 90 percentile. Perkins score is another
983 metric based on the frequency distribution to quantify the similarity between observed
984 and modeled distribution. b) Fraction of cumulative distribution as a function of number of
985 wettest days. Unevenness gauges the number of wettest days for half of annual
986 precipitation. FracPRdays measures the fraction of the number of precipitating
987 ($\geq 1\text{mm/day}$) days a year. SDII is designed to measure daily precipitation intensity by
988 annual total precipitation divided by FracPRdays.

989
990
991
992
993
994
995
996
997
998
999
1000

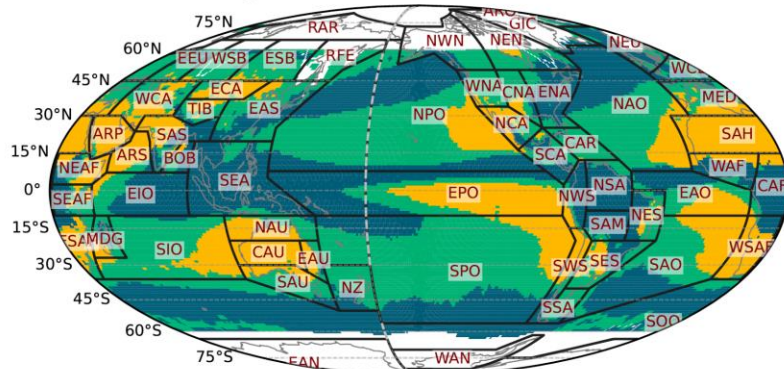
1001
1002
1003
1004



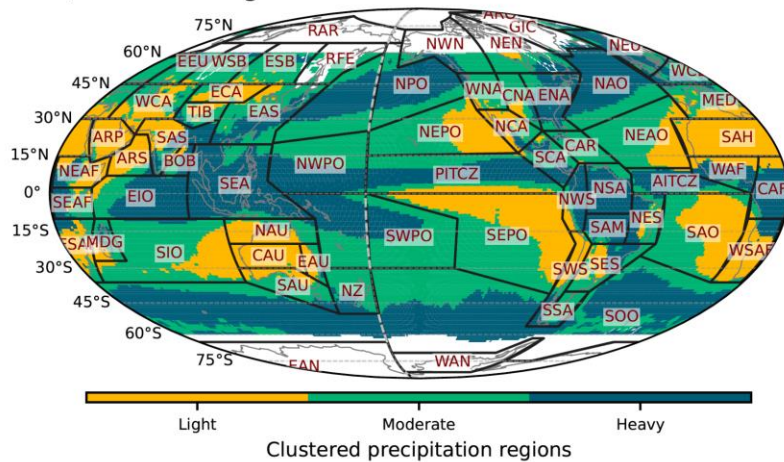
1005
1006
1007 Figure 2. Spatial patterns of IMERG precipitation a) mean state and b) clustering for
1008 heavy, moderate, and light precipitating regions by K-means clustering with amount and
1009 frequency distributions. Precipitation c) amount and d) frequency distributions as a
1010 function of rain rate. Different colors indicate different clustering regions as the same
1011 with b). Thin and thick curves respectively indicate distributions at each grid and the
1012 cluster average.
1013
1014
1015
1016
1017
1018
1019
1020
1021
1022
1023

1024
1025
1026
1027

a) IPCC AR6 regions



b) IPCC AR6 regions with modified ocean

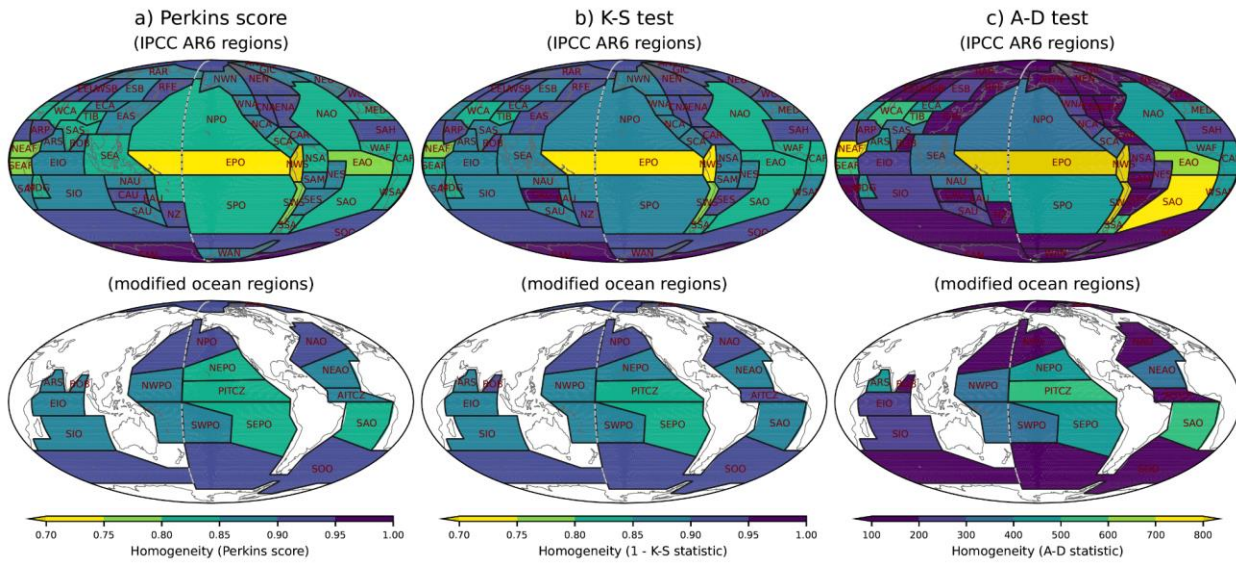


1028

1030 Figure 3. a) IPCC AR6 climate reference regions and b) modified IPCC AR6 climate
1031 reference regions superimposed on the precipitation distributions clustering map shown
1032 in Fig. 2b. Land regions are the same between a) and b), while some ocean regions are
1033 modified.

1034
1035
1036
1037
1038
1039
1040
1041
1042

1043
1044
1045
1046

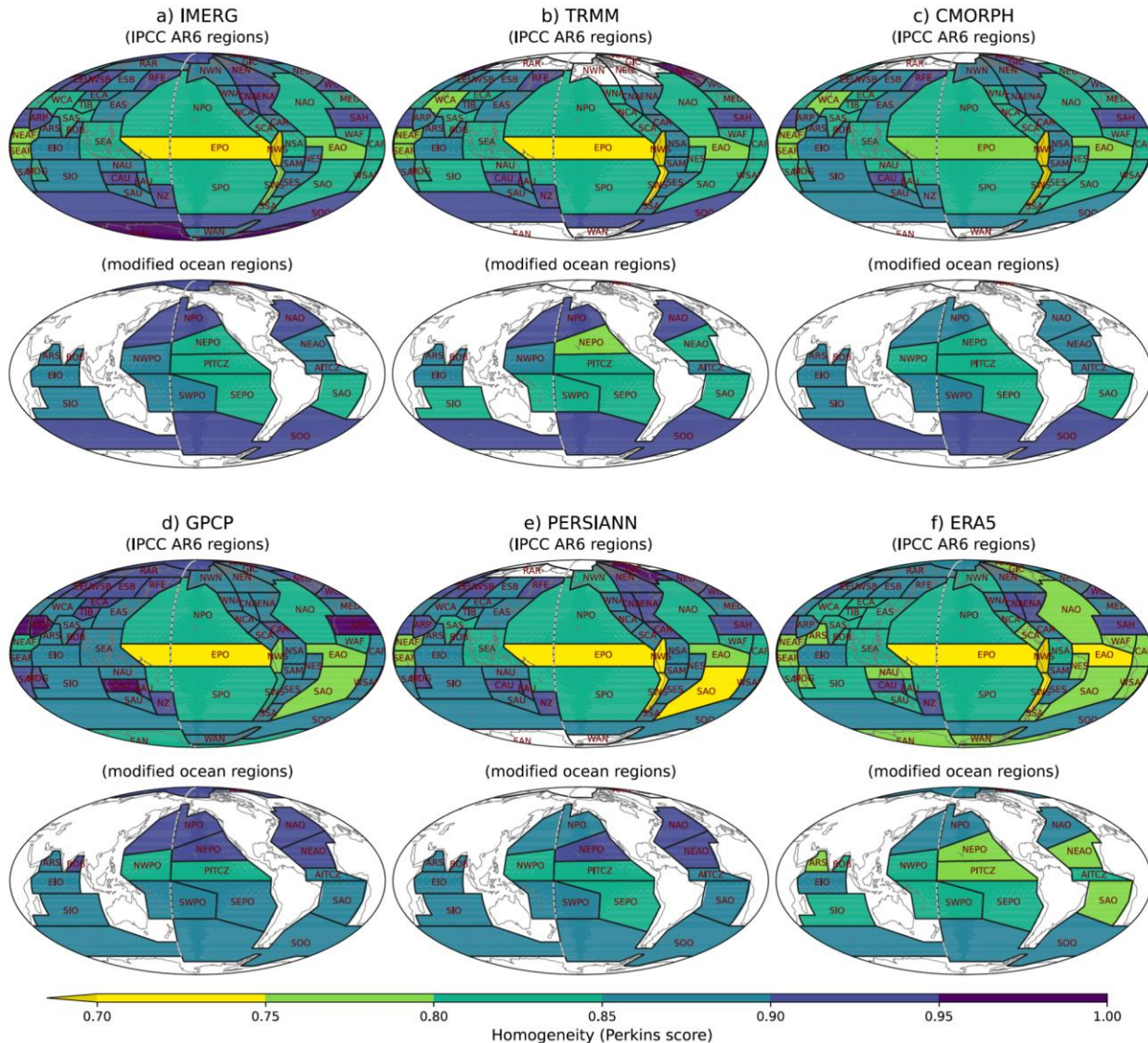


1047
1048

1049 Figure 4. Homogeneity estimated by a) Perkins score, b) K-S test, and c) A-D test
1050 between the region averaged and each grid's frequency distributions of IMERG
1051 precipitation for the IPCC AR6 climate reference regions (upper) and the modified
1052 ocean regions (bottom). Darker color indicates higher homogeneity across all panels.

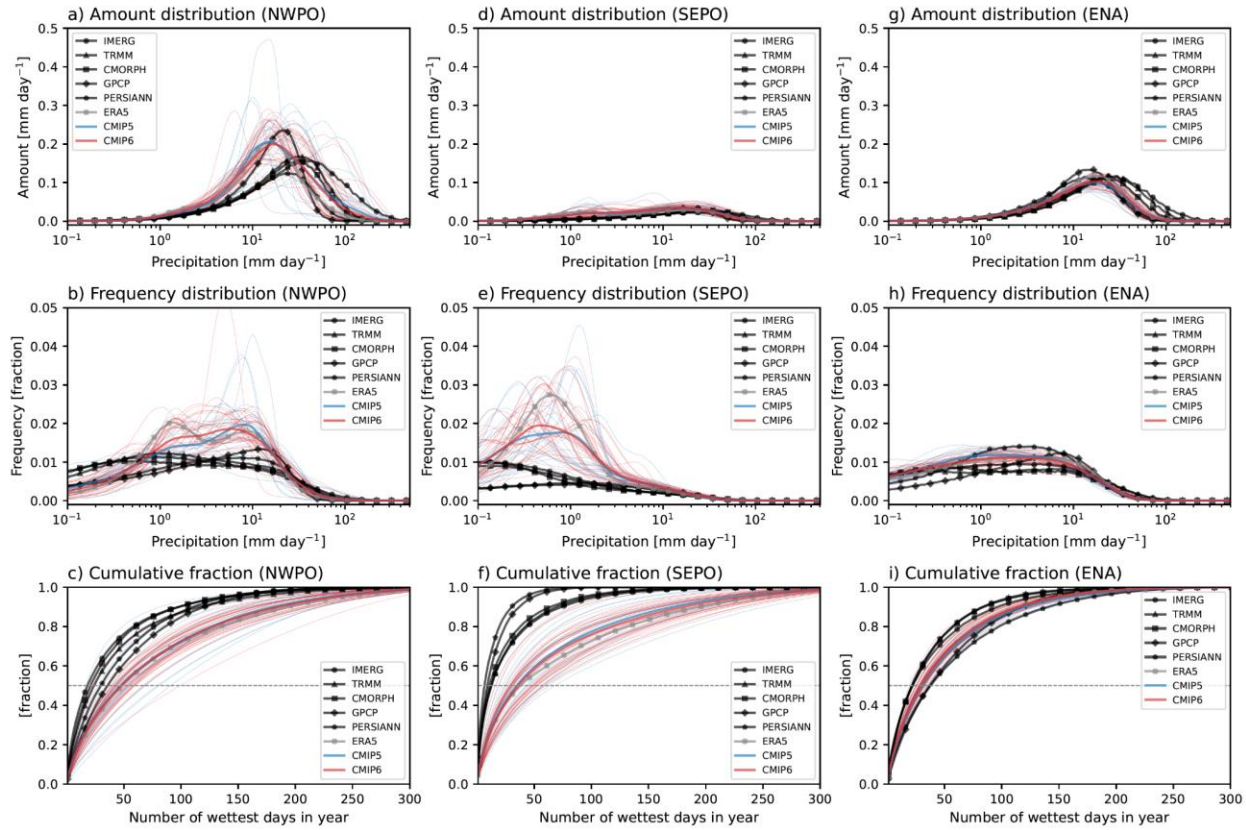
1053
1054
1055
1056
1057
1058
1059
1060
1061
1062
1063
1064
1065
1066
1067
1068
1069
1070

1071
1072
1073
1074



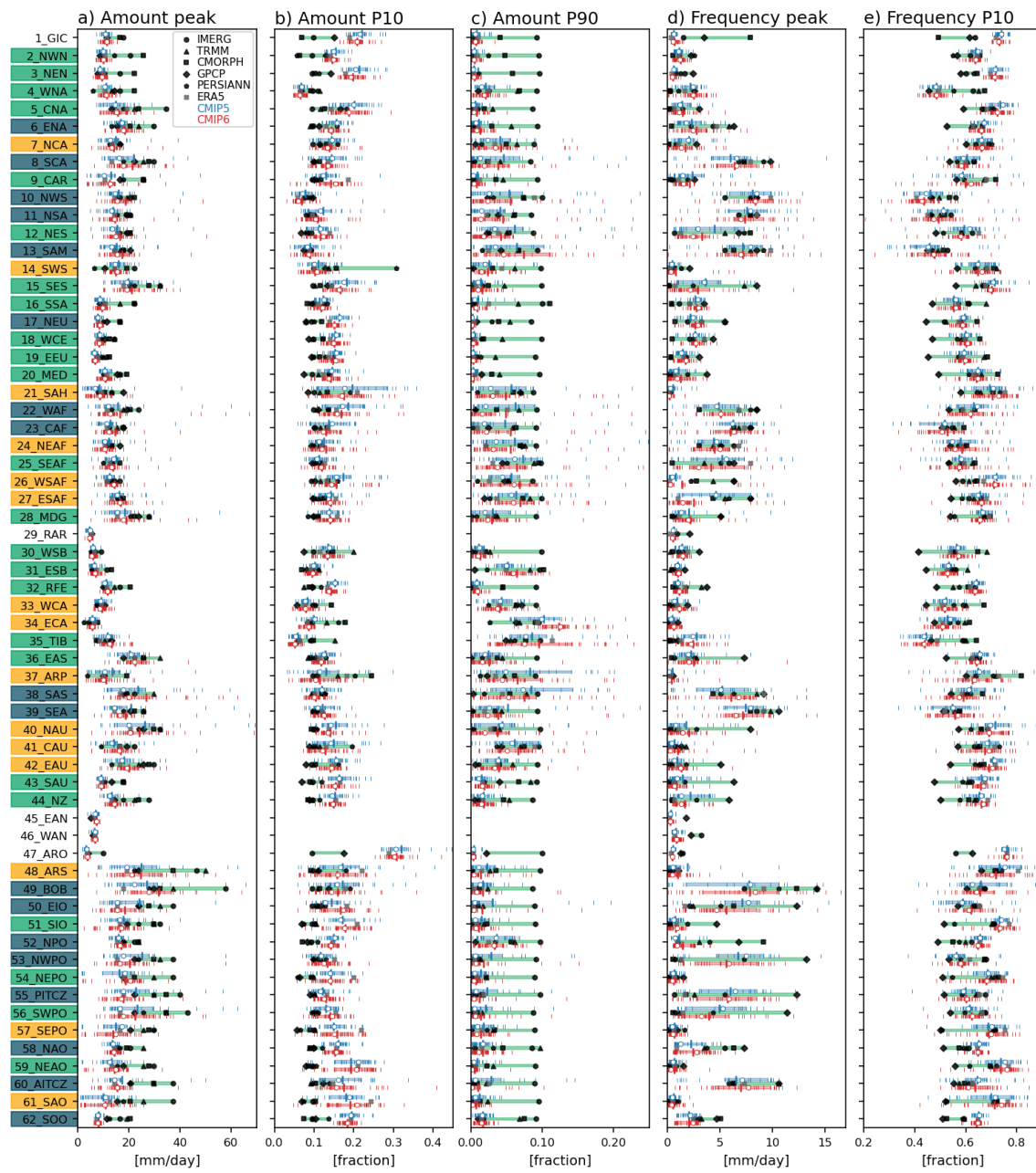
1075
1076
1077 Figure 5. As in Fig. 4, but for different observational datasets with Perkins score.
1078
1079
1080
1081
1082
1083
1084
1085

1086
1087
1088
1089



1090
1091
1092 Figure 6. Precipitation amount (upper), frequency (middle), and cumulative (bottom)
1093 distributions for a-c) NWPO, b-f) SEPO, and g-j) ENA. Black, gray, blue, and red curves
1094 indicate the satellite-based observations, reanalysis, CMIP5 models, and CMIP6
1095 modes, respectively. Thin and thick curves for CMIP models respectively indicate
1096 distributions for each model and multi-model average. Gray dotted lines in the
1097 cumulative distributions indicate a fraction of 0.5. Note: all model output and
1098 observations were conservatively regridded to 2° in the first step of analysis.
1099
1100
1101
1102
1103
1104
1105
1106
1107

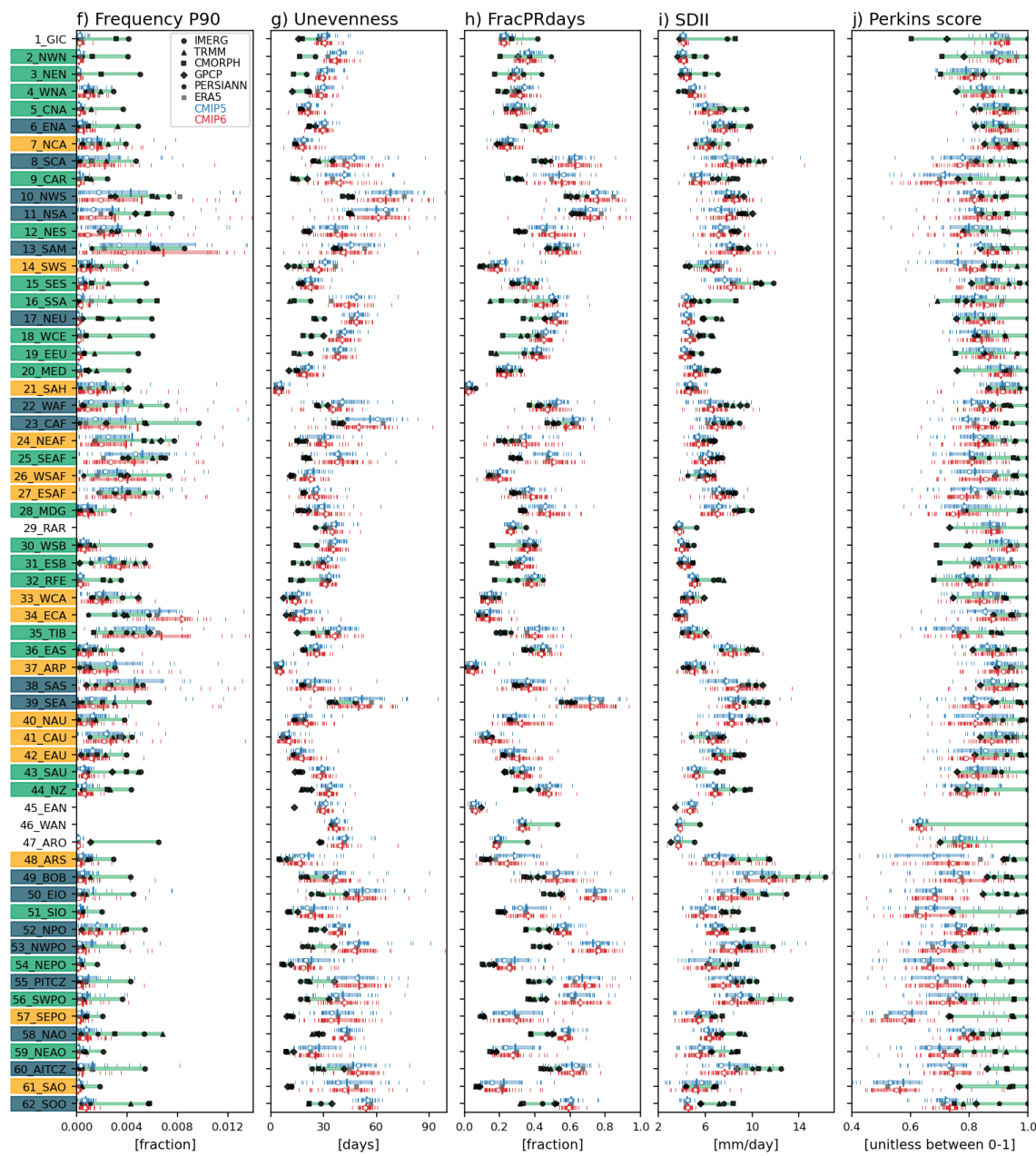
1108
1109
1110



1111
1112

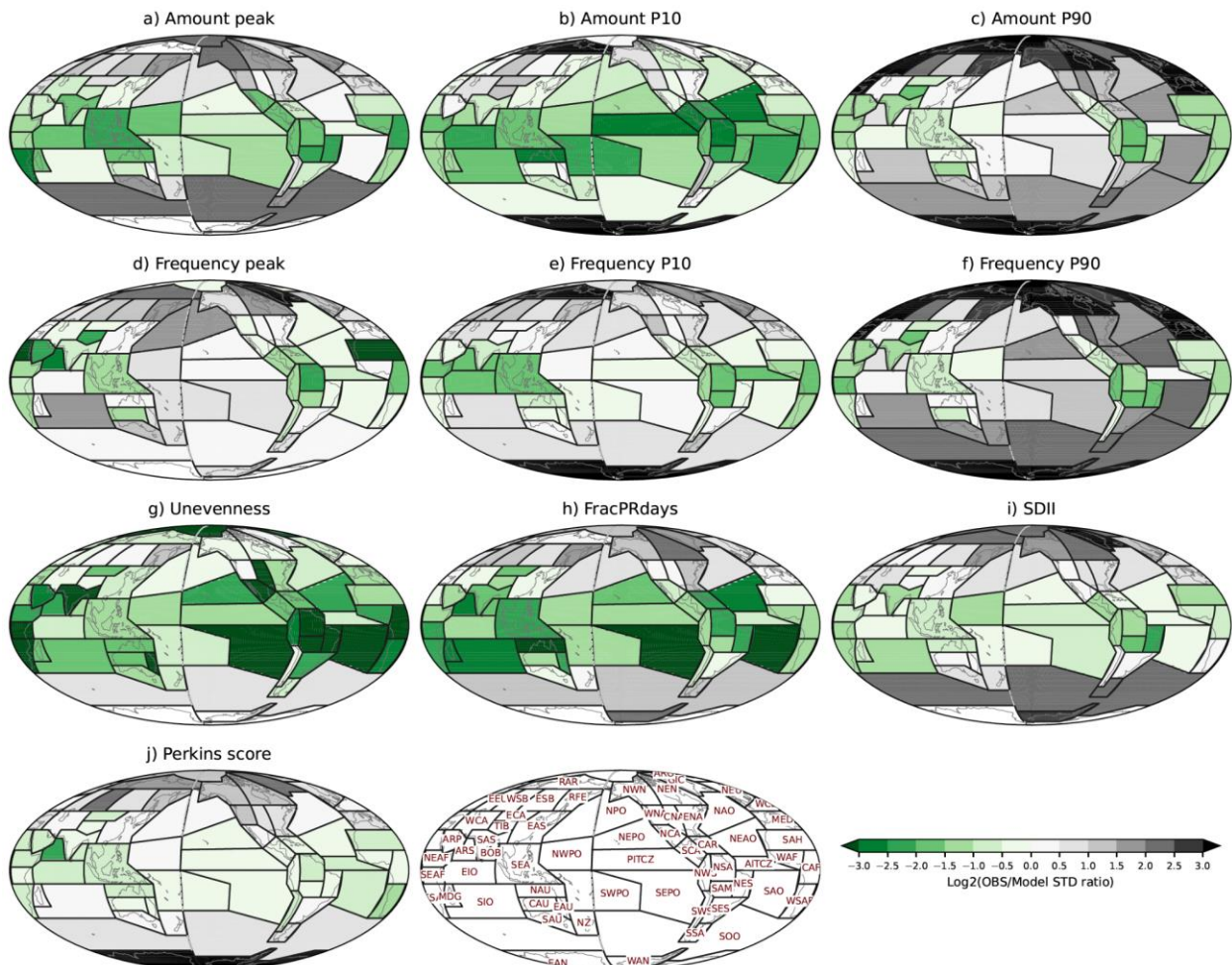
1113 Figure 7. Precipitation distribution metrics for a) Amount peak, b) Amount P10, c)
1114 Amount P90, d) Frequency peak, e) Frequency P10, f) Frequency P90, g) Unevenness,
1115 h) FracPRdays, i) SDII, and j) Perkins score over the modified IPCC AR6 regions.
1116 Black, gray, blue, and red markers indicate the satellite-based observations, reanalysis,
1117 CMIP5 models, and CMIP6 modes, respectively. Thin and thick vertical marks for CMIP
1118 models respectively indicate distributions for each model and multi-model average.

1119 Open circle mark for CMIP models indicates the multi-model median. Green shade
 1120 represents the range between the minimum and maximum values of satellite-based
 1121 observations. Blue and red shades respectively represent the range between 25th and
 1122 75th model values for CMIP 5 and 6 models. Y-axis labels are shaded with the three
 1123 colors as the same in Fig. 2b, indicating dominant precipitating characteristics. Note that
 1124 regions 1-46 are land and land-ocean mixed regions, and 47-62 are ocean regions.
 1125
 1126



1127
 1128
 1129 Figure 7. (continued)

1130
1131
1132

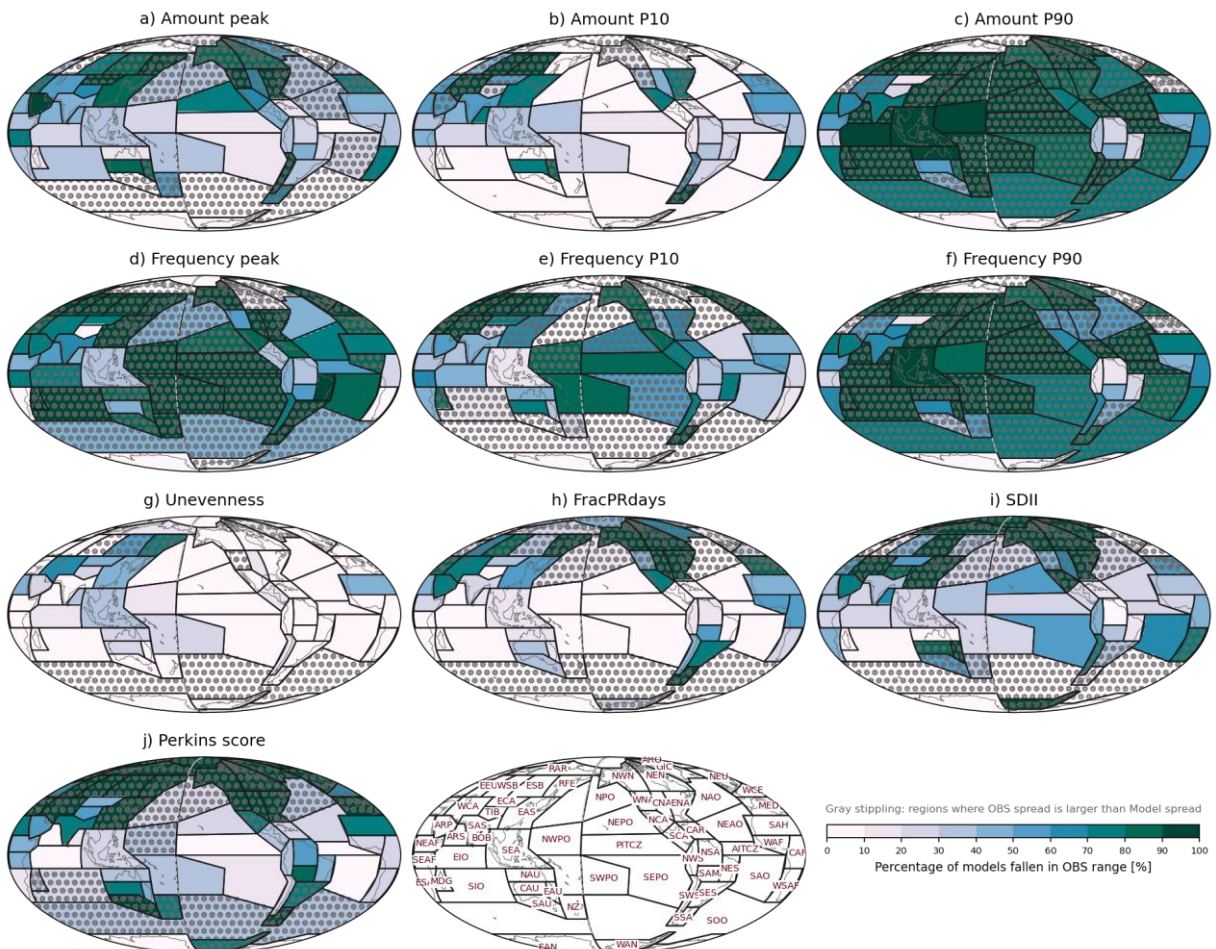


1133
1134

1135 Figure 8. Observational discrepancies relative to spread in the multi-model ensemble for
1136 a) Amount peak, b) Amount P10, c) Amount P90, d) Frequency peak, e) Frequency
1137 P10, f) Frequency P90, g) Unevenness, h) FracPRdays, i) SDII, and j) Perkins score
1138 over the modified IPCC AR6 regions. The observational discrepancy is calculated by
1139 the standard deviation of satellite-based observations divided by the standard deviation
1140 of CMIP 5 and 6 models for each metric and region.

1141
1142
1143
1144
1145
1146
1147

1148
1149
1150

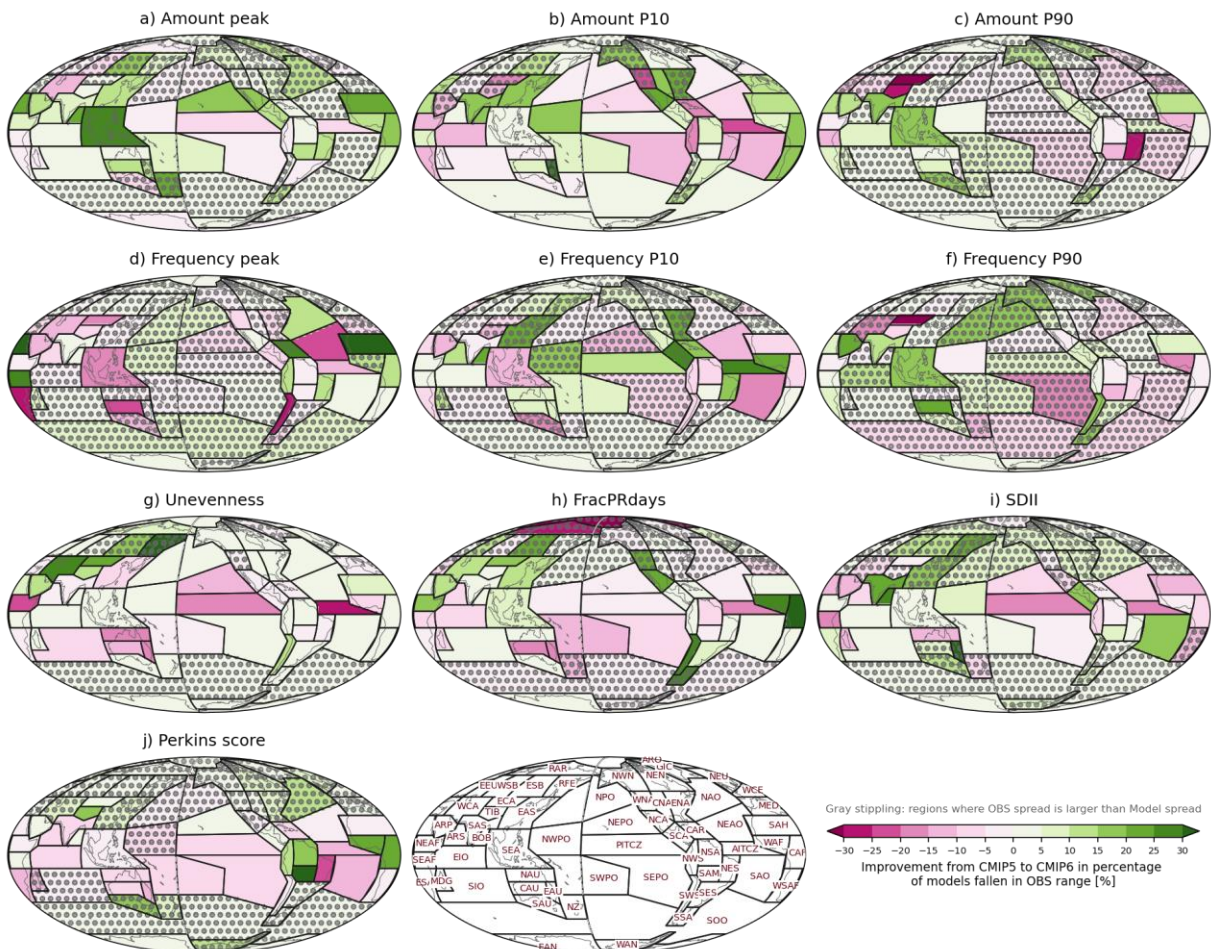


1151
1152

1153 Figure 9. Percentage of CMIP6 models within range of the observational products for a)
1154 Amount peak, b) Amount P10, c) Amount P90, d) Frequency peak, e) Frequency P10, f)
1155 Frequency P90, g) Unevenness, h) FracPRdays, i) SDII, and j) Perkins score over the
1156 modified IPCC AR6 regions. The observational range is between the minimum and
1157 maximum values of five satellite-based products. Regions where the observational
1158 spread is larger than model spread shown in Fig. 8 are stippled gray.

1159
1160
1161
1162
1163
1164
1165
1166

1167
1168
1169

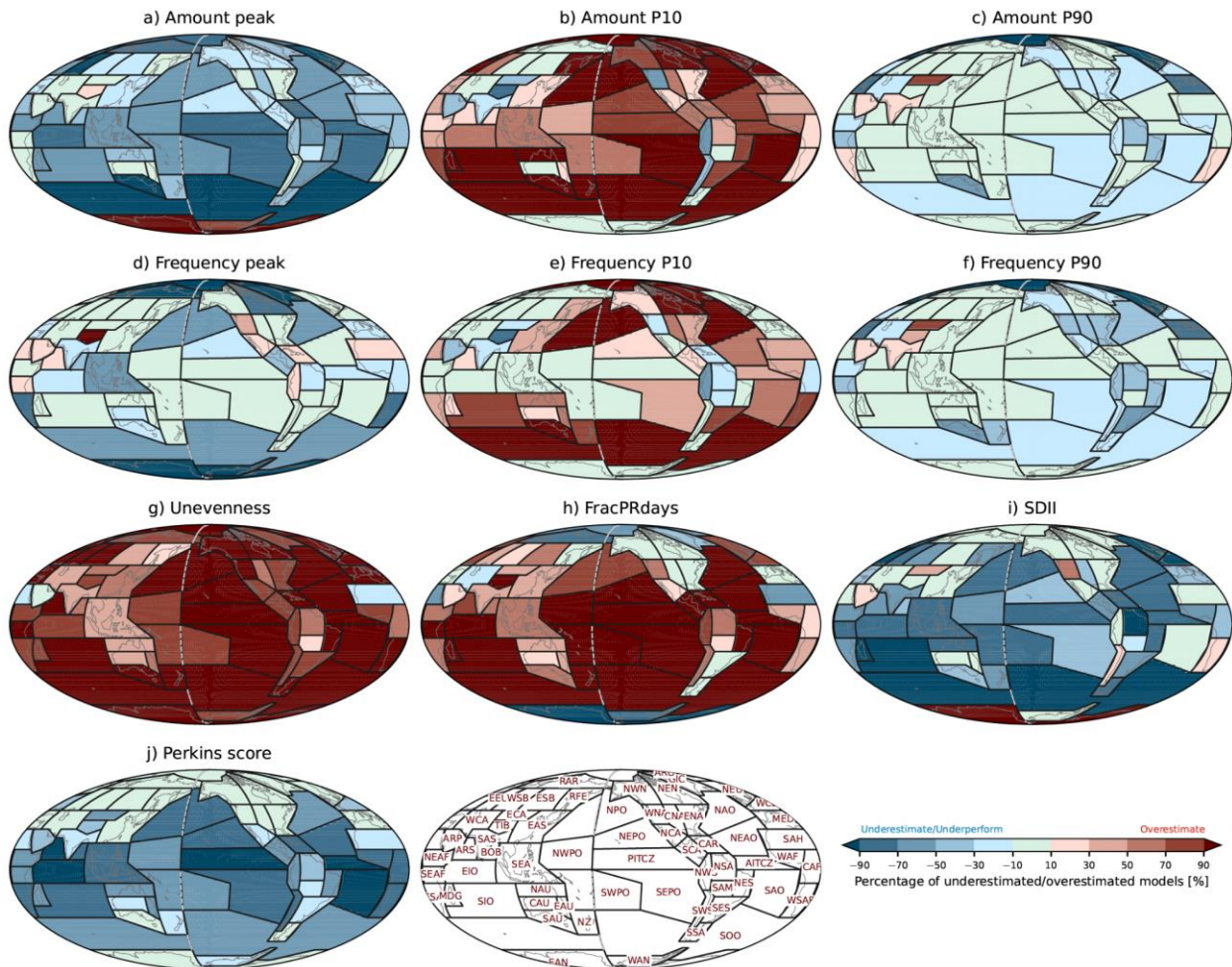


1170
1171

1172 Figure 10. Improvement from CMIP 5 to 6 as identified by the percentage of models in
1173 each multi-model ensemble that are within the observational min-to-max range. The
1174 improvement is calculated by the CMIP6 percentage minus the CMIP5 percentage, so
1175 that positive and negative values respectively indicate improvement and deterioration in
1176 CMIP6. Regions where the observational spread is larger than model spread are
1177 stippled gray.

1178
1179
1180
1181
1182
1183
1184
1185

1186
1187
1188

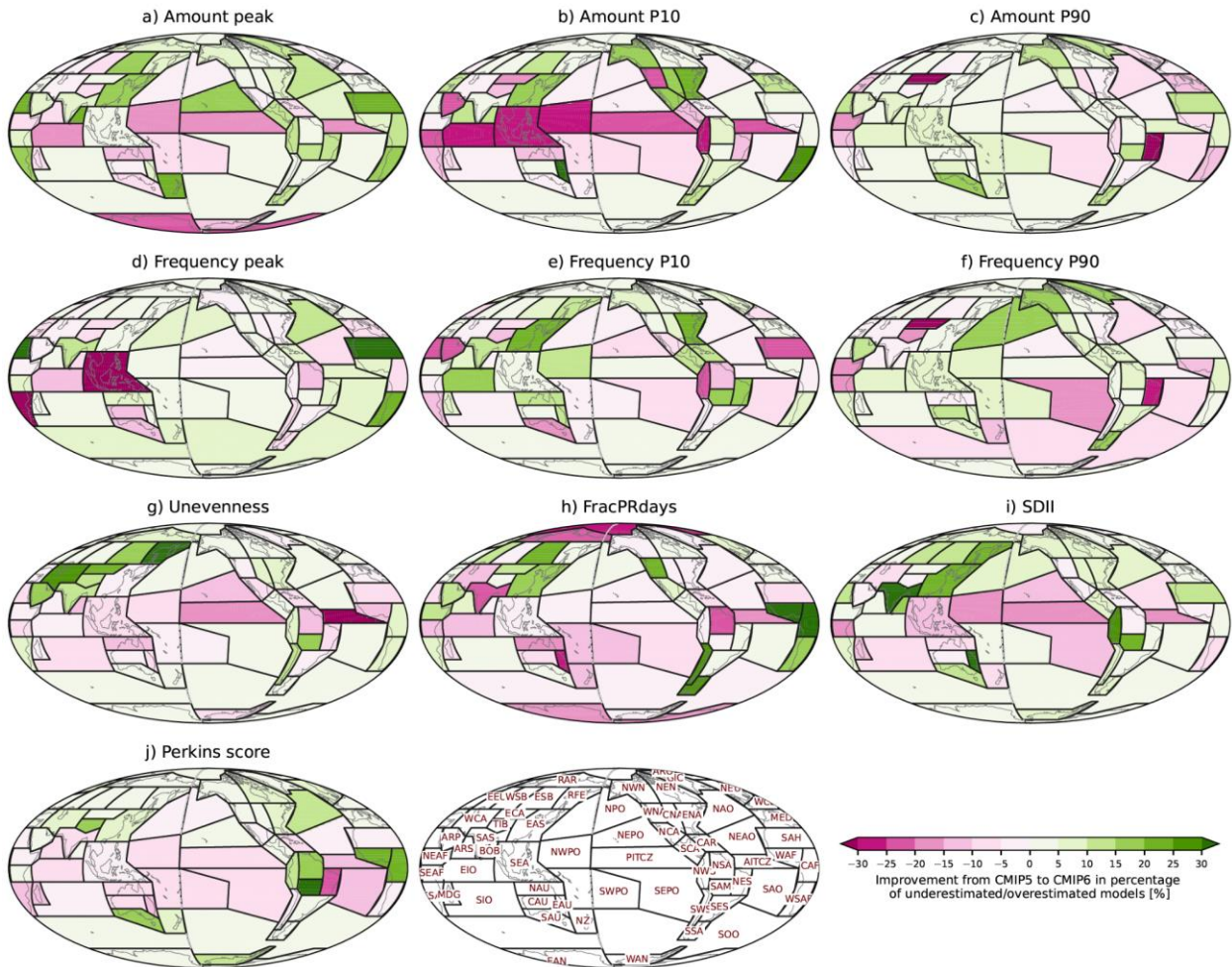


1189
1190

1191 Figure 11. Percentage of CMIP6 models underestimating or overestimating
1192 observations for a) Amount peak, b) Amount P10, c) Amount P90, d) Frequency peak,
1193 e) Frequency P10, f) Frequency P90, g) Unevenness, h) FracPRdays, i) SDII, and j)
1194 Perkins score over the modified IPCC AR6 regions. The criteria for underestimation and
1195 overestimation are respectively defined by minimum and maximum values of satellite-
1196 based observations shown in Fig. 7. Positive and negative values respectively represent
1197 overestimation and underestimation by a formulation of $(nO - nU)/nT$ where nO, nU, nT
1198 are respectively the number of overestimated models, underestimated models, and total
1199 models.

1200
1201
1202
1203

1204
1205
1206



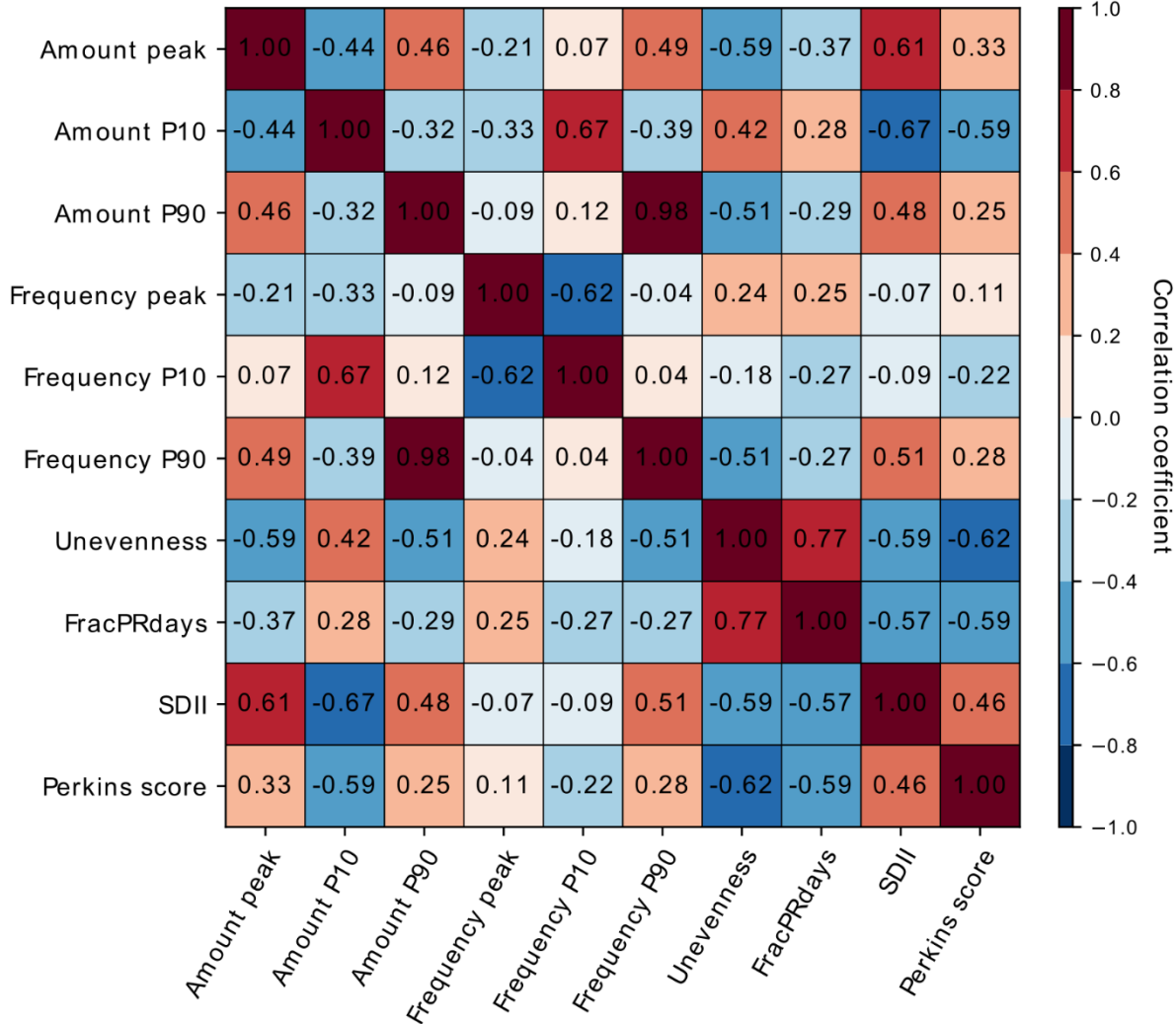
1207
1208

Figure 12. Improvement from CMIP 5 to 6 in the percentage of underestimated or overestimated models. The improvement is calculated by the absolute value of CMIP5 percentage minus the absolute value of CMIP6 percentage, so that positive and negative values respectively indicate improvement and deterioration in CMIP6.

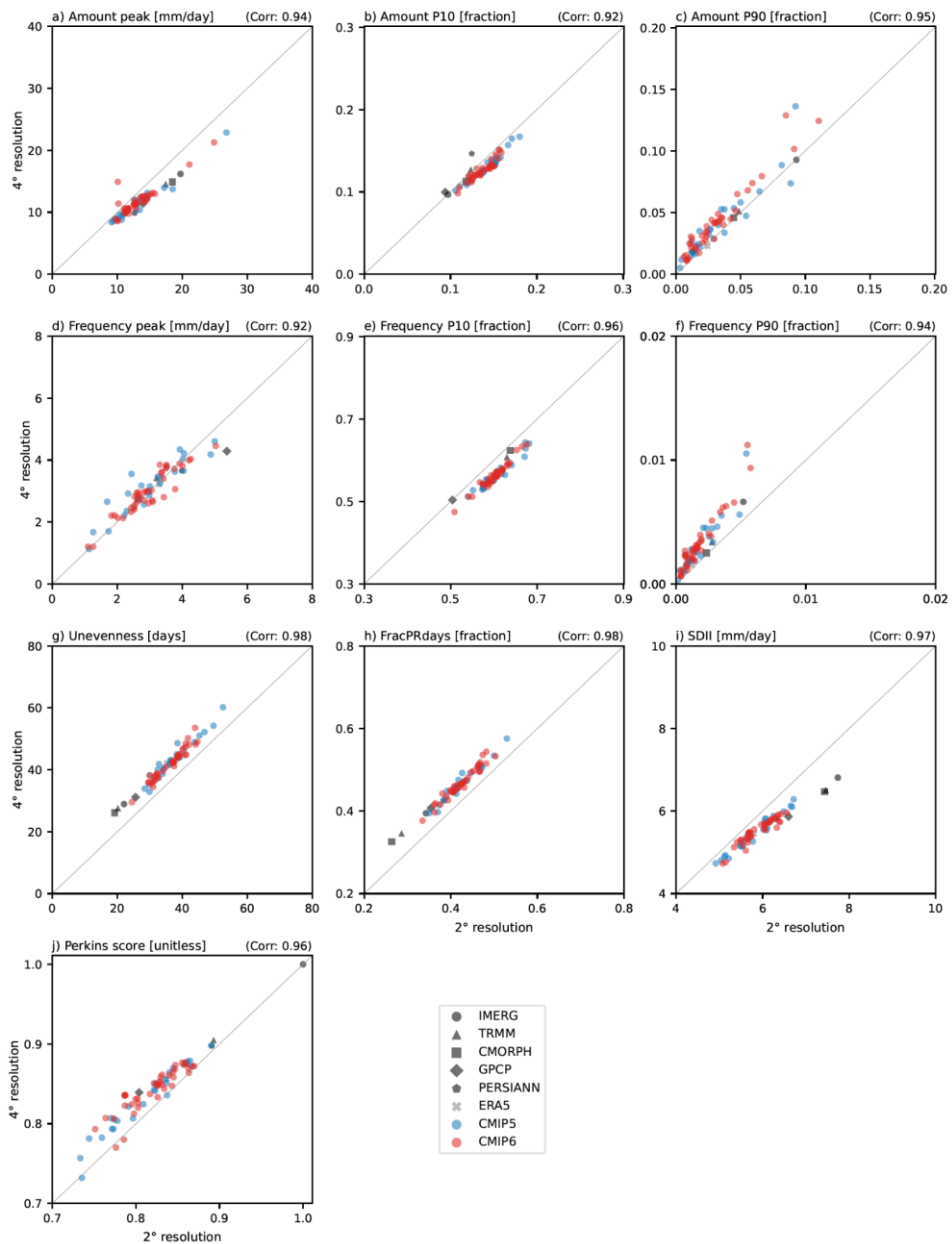
1213
1214
1215
1216
1217
1218
1219
1220
1221

1222
1223
1224

Correlation between precip distribution metrics



1225
1226
1227 Figure 13. Correlation between precipitation distribution metrics across CMIP 5 and 6
1228 model performances. The correlation coefficients are calculated for the modified IPCC
1229 AR6 regions and then area-weighted averaged globally.
1230
1231
1232
1233
1234
1235
1236



1240 Figure 14. Scatterplot between 2° and 4° interpolated horizontal resolutions in
 1241 evaluating precipitation distribution metrics for a) Amount peak, b) Amount P10, c)
 1242 Amount P90, d) Frequency peak, e) Frequency P10, f) Frequency P90, g) Unevenness,
 1243 h) FracPRdays, i) SDII, and j) Perkins score. The metric values are calculated for the
 1244 modified IPCC AR6 regions and then weighted averaged globally. Black, gray, blue, and
 1245 red marks indicate the satellite-based observations, reanalysis, CMIP5 models, and
 1246 CMIP6 modes, respectively. The number in the upper right of each panel is the
 1247 correlation coefficient between the metric values in 2° and 4° resolutions across all
 1248 observations and models.

1249

1250